

Unusual electronic structure in underdoped cuprate superconductors

Xiang Li^{1,2}, Minghuan Zeng³, Huaiming Guo⁴, and Shiping Feng^{2,1*}

¹*School of Physics and Astronomy, Beijing Normal University, Beijing 100875, China*

²*Department of Physics, Faculty of Arts and Sciences,
Beijing Normal University, Zhuhai 519087, China*

³*College of Physics, Chongqing University, Chongqing 401331, China and*

⁴*School of Physics, Beihang University, Beijing 100191, China*

The underdoped cuprate superconductors are characterized by the opening of the normal-state pseudogap, while such an aspect of the normal-state pseudogap effect should be reflected in the low-energy electronic structure. Here the effect of the normal-state pseudogap on the low-energy electronic structure in the underdoped cuprate superconductors is investigated within the framework of the kinetic-energy-driven superconductivity. The strong coupling of the electrons with the spin excitation induces the normal-state pseudogap-state in the particle-hole channel and superconducting (SC) state in the particle-particle channel, where the normal-state pseudogap and SC gap respectively originate from the electron normal and anomalous self-energies, and are evaluated by taking into account the vertex correction. As a natural consequence of the interplay between the normal-state pseudogap-state and SC-state, the SC transition temperature T_c exhibits a dome-like shape of the doping dependence, however, in a striking contrast to T_c in the underdoped regime, the normal-state pseudogap crossover temperature T^* is much higher than T_c in the underdoped regime, and then it decreases with the increase of doping, eventually disappearing together with T_c at the end of the SC dome. Concomitantly, the spectral weight on the electron Fermi surface (EFS) at around the antinodal region is suppressed strongly by this normal-state pseudogap, and then EFS is truncated to form four disconnected Fermi arcs centered around the nodal region with the largest spectral weight located at around the tips of the disconnected Fermi arcs. Moreover, the dip in the peak-dip-hump structure observed in the energy distribution curve and checkerboard charge ordering found in the ARPES autocorrelation are intrinsically connected with the emergence of the normal-state pseudogap. The theory therefore indicates that the same spin excitation that governs both the normal-state pseudogap-state and SC-state naturally leads to the exotic features of the low-energy electronic structure in the underdoped cuprate superconductors.

PACS numbers: 74.25.Jb, 74.25.Dw, 74.20.Mn, 74.20.-z

Keywords: Electronic structure; Normal-state pseudogap; Peak-dip-hump structure; Checkerboard charge ordering; Cuprate superconductor

I. INTRODUCTION

In the conventional superconductors^{1,2}, only an energy gap emerges in the quasiparticle excitation spectrum below the superconducting (SC) transition temperature T_c . This energy gap is corresponding to the energy to break an electron pair, and therefore is identified as the electron-pair gap or the SC gap. As in the case of the conventional superconductors^{1,2}, the pairing of electrons in the cuprate superconductors occurs at T_c , creating the SC gap that serves as the SC-state order parameter³⁻⁵. However, in a stark contrast to the conventional superconductors^{1,2}, a distinct energy gap called the normal-state pseudogap⁶⁻¹⁶ exists above T_c but below the normal-state pseudogap crossover temperature T^* . In particular, this normal-state pseudogap is most notorious in the underdoped regime, where the charge-carrier doping concentration is too low for the optimal superconductivity. This is why in the underdoped regime, the phase above T_c but below T^* is so-called as *the normal-state pseudogap phase*. This normal-state pseudogap is the most noteworthy, which suppresses strongly the electronic density of states on the electron Fermi surface (EFS), and then the physical response in the underdoped

regime can be well interpreted in terms of the formation of this normal-state pseudogap.

By virtue of systematic studies using angle-resolved photoemission spectroscopy (ARPES) measurement techniques, a number of consequences from the effect of the normal-state pseudogap on the low-energy electronic structure together with the associated exotic phenomena have been identified experimentally in the underdoped regime, where the main characteristic features can be summarized as: (i) the stronger quasiparticle scattering is observed at around the antinodal region than at around the nodal region, this leads to the formation of the disconnected Fermi arcs centered at around the nodal region¹⁷⁻²⁵. In particular, one of the intrinsic features associated with this EFS instability is the emergence of the multiple nearly-degenerate electronic orders²⁵⁻³⁰; (ii) the dramatic change in the line-shape of the energy distribution curve is detected³¹⁻⁴⁰, where a sharp quasiparticle peak develops at low binding energies, followed by a dip and a hump, giving rise to the so-called peak-dip-hump (PDH) structure; (iii) the sharp peaks in the ARPES autocorrelation spectrum in the SC-state with the scattering wave vectors \mathbf{q}_i are directly correlated with the regions of the highest joint density of

states^{41–43}, where scattering wave vectors \mathbf{q}_i connect the tips of the Fermi arcs obeying an *octet scattering model*. Since the anomalous properties, including the exceptionally strong superconductivity, have often been attributed to the particular characteristics of the low-energy electronic structure^{10–12}, the understanding of the effect of the normal-state pseudogap on the low-energy electronic structure in the underdoped cuprate superconductors is thought to be key to the understanding of the nonconventional mechanism of superconductivity.

Although the exotic features of the low-energy electronic structure in the underdoped cuprate superconductors have been established experimentally, a complete understanding of these exotic features is still unclear. After intensive investigations over three decades, a large body of experimental evidence has shown that as in the case of the SC-state^{44,45}, the normal-state pseudogap-state may also originate from the electron interaction mediated by a particular bosonic mode^{6–16}. In this case, a key question is whether a common bosonic excitation, which mediates the interaction between electrons responsible for both the SC-state and normal-state pseudogap-state, generates the anomalous properties of the electronic structure. In the previous works^{46–48}, the low-energy electronic structure in the cuprate superconductors has been discussed within the framework of the kinetic-energy-driven superconductivity, where both the electron normal self-energy in the particle-hole channel and electron anomalous self-energy in the particle-particle channel generated by the coupling of the electrons with the spin excitation are evaluated, and employed to study the renormalization of the electrons. However, these calculations^{46–48} suffer from ignoring the vertex correction for the electron normal and anomalous self-energies, while the influence of the vertex correction may be dramatic in the underdoped regime. In this paper, we study the low-energy electronic structure in the underdoped cuprate superconductors along with this line^{46–48} by taking into account the vertex correction for the electron normal and anomalous self-energies, where we show clearly that (i) the normal-state pseudogap and SC gap respectively originate from the electron normal self-energy in the particle-hole channel and anomalous self-energy in the particle-particle channel, and then the SC-state coexists and competes with the normal-state pseudogap-state below T_c over the whole SC dome. This leads to that although T_c takes a dome-like shape with the underdoped and the overdoped regimes on each side of the optimal doping, where T_c reaches its maximum, T^* is much higher than T_c in the underdoped regime, and then it gradually merges with the SC gap in the strongly overdoped region; (ii) the characteristic features of the low-energy electronic structure observed from the ARPES experiments, including the EFS reconstruction^{17–25}, the nature of the charge-order correlation^{25–30}, the striking PDH structure in the energy distribution curve^{31–40}, and the remarkable ARPES autocorrelation spectrum^{41–43}, are qualitatively reproduced. In particular, in addition to these sharp peaks

in the ARPES autocorrelation spectrum with the scattering wave vectors \mathbf{q}_i , the notable checkerboard peaks appear only in the normal-state pseudogap phase, and are directly linked with the opening of the normal-state pseudogap. Our results therefore also indicate that the *same spin excitation* that governs both the normal-state pseudogap-state and the SC-state naturally generates the exotic features of the low-energy electronic structure in the underdoped cuprate superconductors.

This paper is organized as follows. The theoretical framework is presented in Section II, where the full electron diagonal and off-diagonal propagators obtained by taking into account the vertex correction are given. Starting from these full electron diagonal and off-diagonal propagators, the phase diagram of the cuprate superconductors is derived for a convenience in the discussion of the low-energy electronic structure in the underdoped cuprate superconductors. The quantitative characteristics of the low-energy electronic structure are presented in Section III, where we show that the scattering wave vector of the notable checkerboard charge ordering found in the ARPES autocorrelation in the normal-state pseudogap phase is well consistent with that observed from the ARPES and scanning tunneling spectroscopy (STS) experiments. Finally, we give a summary in Sec. IV. In Appendix A, we present the generalization of the main formalisms of the kinetic-energy-driven superconductivity from the case with the neglect of the vertex correction for the electron normal and anomalous self-energies to the present case by the inclusion of the vertex correction, where the detail of the calculation of the phase diagram is given.

II. METHODOLOGY

A. Model and electron local constraint

The basic element of the crystal structure in cuprate superconductors is the two-dimensional CuO_2 plane^{3,4} in which superconductivity with the exceptionally high T_c appears upon charge-carrier doping. Soon after the discovery of superconductivity in cuprate superconductors, Anderson⁴⁹ recognized that the essential physics of cuprate superconductors can be properly depicted in terms of the t - J model on a square lattice,

$$H = - \sum_{l'l'\sigma} t_{ll'} C_{l\sigma}^\dagger C_{l'\sigma} + \mu \sum_{l\sigma} C_{l\sigma}^\dagger C_{l\sigma} + J \sum_{\langle ll' \rangle} \mathbf{S}_l \cdot \mathbf{S}_{l'}, \quad (1)$$

where $C_{l\sigma}^\dagger$ ($C_{l\sigma}$) creates (annihilates) an electron with spin index σ on lattice site l , \mathbf{S}_l is a localized spin operator with its components S_l^x , S_l^y , and S_l^z , and μ is the chemical potential. The kinetic-energy term consists of the constrained electron hopping between the nearest-neighbor (NN) sites $\hat{\eta}$ with the hopping integral $t_{ll'} = t_{\hat{\eta}} = t$ and the constrained electron hopping between the next NN sites $\hat{\tau}$ with the hopping integral

$t_{ll'} = t_{\hat{\tau}} = -t'$, while the magnetic-energy term consists of the magnetic interaction between the NN sites $\hat{\eta}$ with the magnetic exchange coupling J . The summation ll' indicates that l runs over all sites, and for each l , over its NN sites $\hat{\eta}$ and next NN sites $\hat{\tau}$, while the summation $\langle ll' \rangle$ is taken over all the NN pairs. In the following discussions, the NN magnetic exchange coupling J and the lattice constant of the square lattice are respectively set as the energy and length units, while t and t' are respectively set to be $t/J = 2.5$ and $t'/t = 0.3$, which are the typical values of cuprate superconductors^{10–12}. In particular, when necessary to compare with the experimental data, we set $J = 100\text{meV}$.

The t - J model (1) is the strong-coupling limit of the Hubbard model, and then the difficulty of its solution lies in enforcing the no double electron occupancy on-site local constraint^{50–54}, i.e., $\sum_{\sigma} C_{l\sigma}^{\dagger} C_{l\sigma} \leq 1$. An intuitively appealing approach to implement this on-site local constraint is the slave-particle approach^{50–53}, where the constrained electron operator is decoupled as $C_{l\sigma} = a_l^{\dagger} f_{l\sigma}$ with a_l^{\dagger} as the slave boson and $f_{l\sigma}$ as the spinful fermion and the on-site local constraint $\sum_{\sigma} f_{l\sigma}^{\dagger} f_{l\sigma} + a_l^{\dagger} a_l = 1$, or *vice versa*, i.e., a_l^{\dagger} as the fermion and $f_{l\sigma}$ as the boson. Due to the on-site local constraint, these particles are also coupled by a strong $U(1)$ gauge field^{50,53}, allowed in this slave-particle representation. However, there are a number of difficulties in this approach. First of all, in the slave-boson version, the antiferromagnetic correlation is absent for zero doping, so the ground-state energy is high compared with the numerical estimation for small clusters, and the Marshall sign-rule is not obeyed. Alternatively, in the slave-fermion approach, the ground-state is antiferromagnetic for the undoped case and persists until very high doping ($\sim 60\%$). In particular, if we, following the common practice, let $f_{l\sigma}$ keep track of the spin degree of freedom of the constrained electron, while a_l keep track of the charge degree of freedom of the constrained electron, satisfying the sum rules: $\delta = \langle a_l^{\dagger} a_l \rangle$ and $1 - \delta = \sum_{\sigma} \langle f_{l\sigma}^{\dagger} f_{l\sigma} \rangle$, where δ is the charge-carrier doping concentration, we⁵¹ find that the sum rule for the physical electron $\sum_{\sigma} \langle C_{l\sigma}^{\dagger} C_{l\sigma} \rangle = 1 - \delta$ is not satisfied for both versions. Moreover, we⁵¹ have also shown that the overall electron distribution does not have the appropriate EFS within this scheme. These are intrinsic difficulties of this decoupling scheme. To avoid these difficulties in the slave-particle approach, the method employed to analyse the t - J model (1) together with the on-site local constraint of the no double electron occupancy in this paper is the fermion-spin theory^{55,56}, in which the constrained electron operators $C_{l\uparrow}$ and $C_{l\downarrow}$ in the t - J model (1) are decoupled into two distinct operators as,

$$C_{l\uparrow} = h_{l\uparrow}^{\dagger} S_l^{-}, \quad C_{l\downarrow} = h_{l\downarrow}^{\dagger} S_l^{+}, \quad (2)$$

where $h_{l\sigma}^{\dagger} = e^{i\Phi_{l\sigma}} h_l^{\dagger}$ ($h_{l\sigma} = e^{-i\Phi_{l\sigma}} h_l$) is a spinful fermion creation (annihilation) operator, which creates (annihilates) a charge carrier at site l , and therefore keeps track

of the charge degree of freedom of the constrained electron together with some effects of spin configuration rearrangements due to the presence of the doped charge carrier itself, while S_l^{+} (S_l^{-}) is the spin-raising (spin-lowering) operator, which keeps track of the spin degree of freedom of the constrained electron. The advantages of this fermion-spin approach (2) can be summarized as: (i) the on-site local constraint of no double occupancy is satisfied in actual analyses; (ii) the charge carrier or spin *itself* is $U(1)$ gauge invariant, and then the collective mode for the spin is real and can be interpreted as the spin excitation responsible for the dynamical spin response, while the electron quasiparticle as a result of the charge-spin recombination of a charge carrier and a localized spin is not affected by the statistical $U(1)$ gauge fluctuation, and is responsible for the electronic-state properties. This is why the fermion-spin approach (2) is an efficient calculation scheme which can provide a proper description of the anomalous properties of cuprate superconductors.

B. Interplay between superconducting-state and normal-state pseudogap-state

In a superconductor, the formation of the electron pairs is crucial in the occurrence of superconductivity because the electron pairs behave as effective bosons, and can form something analogous to a Bose condensate that flows without resistance⁵⁷. This follows from a basic fact that although electrons repel each other because of the presence of the Coulomb repulsive interaction, at low energies and low temperatures, there can be an effective attraction originating due to the exchange of boson excitations⁵⁷. In the conventional superconductors, as explained by the Bardeen-Cooper-Schrieffer (BCS) theory^{1,2}, these exchanged boson excitations are *phonons*. These phonons act like a *bosonic glue* to hold the electron pairs together⁵⁸, and then the condensation of these electron pairs reveals the SC-state^{1,2}. However, the BCS theory is not specific to a phonon-mediated interaction between electrons, other bosonic excitations can also serve as the pairing glue^{59,60}. In the past over three decades, a series of experiments from the nuclear magnetic resonance, nuclear quadrupole resonance, inelastic neutron scattering, and resonant inelastic X-ray scattering measurements on the cuprate superconductors^{61–70} have identified the spin excitations with the high intensity over a large part of momentum space. More importantly, these spin excitations exist across the entire range of the SC dome, and with sufficient intensity to mediate superconductivity. In this case, a crucial question is whether the spin excitation can mediate electron pairing in the cuprate superconductors in analogy to the phonon-mediated pairing mechanism in the conventional superconductors? Starting from the fermion-spin theory (2) description of the t - J model (1), we^{56,71–73} have established a kinetic-energy-driven SC mechanism, where the d-wave charge-carrier pairs are

generated by the interaction between charge carriers directly from the kinetic energy of the t - J model by the exchange of the spin excitation, then the d-wave electron pairs originate from the d-wave charge-carrier pairs due to charge-spin recombination⁷³, and these electron pairs condense to form the d-wave SC-state. The mechanism of the kinetic-energy-driven superconductivity is purely electronic without phonon, since the main ingredient is identified into an electron pairing mechanism not involving the phonon, the external degree of freedom, but *the spin excitation, the collective mode from the internal spin degree of freedom of the constrained electron itself*. In other words, the constrained electrons simultaneously act to glue and to be glued^{74,75}. Moreover, this kinetic-energy-driven SC-state in a way is in turn strongly influenced by the single-particle coherence, which leads to that the maximal T_c occurs at around the optimal doping, and then decreases in both the underdoped and overdoped regimes. Our following discussions of the interplay between the SC-state and the normal-state pseudogap-state in the cuprate superconductors builds on the kinetic-energy-driven superconductivity, where the electron normal and anomalous self-energies in this paper are derived by taking into account the vertex correction. For the following discussions of the main physics in the core, the details of the derivation of the main formalisms of the kinetic-energy-driven superconductivity and the related vertex-corrected electron normal and anomalous self-energies are presented in Appendix A. Following our previous discussions⁷³, the full electron diagonal and off-diagonal propagators of the t - J model (1) in the fermion-spin representation (2) can be derived explicitly as [see Appendix A],

$$G(\mathbf{k}, \omega) = \frac{1}{\omega - \varepsilon_{\mathbf{k}} - \Sigma_{\text{tot}}(\mathbf{k}, \omega)}, \quad (3a)$$

$$\mathfrak{S}^\dagger(\mathbf{k}, \omega) = \frac{W(\mathbf{k}, \omega)}{\omega - \varepsilon_{\mathbf{k}} - \Sigma_{\text{tot}}(\mathbf{k}, \omega)}, \quad (3b)$$

where $\varepsilon_{\mathbf{k}} = -4t\gamma_{\mathbf{k}} + 4t'\gamma'_{\mathbf{k}} + \mu$ is the electron energy dispersion in the tight-binding approximation, with $\gamma_{\mathbf{k}} = (\cos k_x + \cos k_y)/2$, and $\gamma'_{\mathbf{k}} = \cos k_x \cos k_y$, while the electron total self-energy $\Sigma_{\text{tot}}(\mathbf{k}, \omega)$ and the function $W(\mathbf{k}, \omega)$ are given explicitly as,

$$\Sigma_{\text{tot}}(\mathbf{k}, \omega) = \Sigma_{\text{ph}}(\mathbf{k}, \omega) + \frac{|\Sigma_{\text{pp}}(\mathbf{k}, \omega)|^2}{\omega + \varepsilon_{\mathbf{k}} + \Sigma_{\text{ph}}(\mathbf{k}, -\omega)}, \quad (4a)$$

$$W(\mathbf{k}, \omega) = -\frac{\Sigma_{\text{pp}}(\mathbf{k}, \omega)}{\omega + \varepsilon_{\mathbf{k}} + \Sigma_{\text{ph}}(\mathbf{k}, -\omega)}, \quad (4b)$$

respectively, with the electron normal self-energy $\Sigma_{\text{ph}}(\mathbf{k}, \omega)$ in the particle-hole channel and electron anomalous self-energy $\Sigma_{\text{pp}}(\mathbf{k}, \omega)$ in the particle-particle channel. In the previous derivations⁴⁶⁻⁴⁸, the electron normal and anomalous self-energies have been calculated with neglecting the vertex correction, where the obtained

results of the electronic structure in the SC-state is qualitatively consistent with the corresponding experimental results observed in the ARPES measurements³¹⁻⁴³, however, the magnitude of the pseudogap gap in the underdoped regime is not large enough compared with the corresponding experimental observations¹⁶, leading to that the electronic density of states on EFS in the underdoped regime is not sufficiently suppressed. This weakness can be corrected in terms of the vertex correction of the electron self-energy⁷⁶. In this paper, for a more proper description of the interplay between the SC-state and normal-state pseudogap-state and the related effect of the normal-state pseudogap on the low-energy electronic structure in the underdoped cuprate superconductors, the above electron normal self-energy $\Sigma_{\text{ph}}(\mathbf{k}, \omega)$ and electron anomalous self-energy $\Sigma_{\text{pp}}(\mathbf{k}, \omega)$ in Eq. (4) can be respectively derived by taking into account the vertex corrections as⁷⁶ [see Appendix A],

$$\begin{aligned} \Sigma_{\text{ph}}(\mathbf{k}, i\omega_n) &= \frac{1}{N^2} \sum_{\mathbf{p}, \mathbf{p}'} [V_{\text{ph}} \Lambda_{\mathbf{p}+\mathbf{p}'+\mathbf{k}}]^2 \\ &\times \frac{1}{\beta} \sum_{ip_m} G(\mathbf{p} + \mathbf{k}, ip_m + i\omega_n) \Pi(\mathbf{p}, \mathbf{p}', ip_m), \end{aligned} \quad (5a)$$

$$\begin{aligned} \Sigma_{\text{pp}}(\mathbf{k}, i\omega_n) &= \frac{1}{N^2} \sum_{\mathbf{p}, \mathbf{p}'} [V_{\text{pp}} \Lambda_{\mathbf{p}+\mathbf{p}'+\mathbf{k}}]^2 \\ &\times \frac{1}{\beta} \sum_{ip_m} \mathfrak{S}^\dagger(\mathbf{p} + \mathbf{k}, ip_m + i\omega_n) \Pi(\mathbf{p}, \mathbf{p}', ip_m), \end{aligned} \quad (5b)$$

where $\Lambda_{\mathbf{k}} = 4t\gamma_{\mathbf{k}} - 4t'\gamma'_{\mathbf{k}}$ is the bare vertex function, while V_{ph} is the vertex correction for the electron normal self-energy, and V_{pp} is the vertex correction for the electron anomalous self-energy, which together with the spin bubble $\Pi(\mathbf{p}, \mathbf{p}', ip_m)$ have been determined explicitly in Appendix A [see Appendix A]. Moreover, the sharp peaks appear at low-temperature in $\Sigma_{\text{ph}}(\mathbf{k}, \omega)$, $\Sigma_{\text{pp}}(\mathbf{k}, \omega)$, and the related quantities that are actually a δ -function, which are broadened by a small damping employed in the numerical calculation for a finite lattice⁷⁷. The calculation in this paper for $\Sigma_{\text{ph}}(\mathbf{k}, \omega)$, $\Sigma_{\text{pp}}(\mathbf{k}, \omega)$, and the related quantities is performed numerically on a 120×120 lattice in momentum space, where the infinitesimal $i0_+ \rightarrow i\Gamma$ is replaced by a small damping $\Gamma = 0.05J$.

Although both the electron normal and anomalous self-energies originate from the coupling of the electrons with the same spin excitation, they capture different aspects of the interaction effect. On the one hand, the SC-state is characterized by the electron anomalous self-energy $\Sigma_{\text{pp}}(\mathbf{k}, \omega)$, which is identified as the energy and momentum dependent electron pair gap (then the SC gap) $\Sigma_{\text{pp}}(\mathbf{k}, \omega) = \bar{\Delta}_{\mathbf{k}}(\omega)$, and thus is corresponding to the energy for breaking an electron pair⁵⁸. In the static limit, this electron pair gap $\bar{\Delta}_{\mathbf{k}}(\omega)$ is reduced as $\bar{\Delta}_{\mathbf{k}}(\omega)|_{\omega=0} = \bar{\Delta}_{\mathbf{k}} = \bar{\Delta}\gamma_{\mathbf{k}}^{(d)}$, with the electron pair gap parameter $\bar{\Delta}$ and the d-wave factor $\gamma_{\mathbf{k}}^{(d)} = (\cos k_x - \cos k_y)/2$ [see Appendix

A]. On the other hand, the single-particle coherence is dominated by the electron normal self-energy $\Sigma_{\text{ph}}(\mathbf{k}, \omega)$, which gives rise to a main contribution to the energy and lifetime renormalization of the electrons, and then all the anomalous properties of the cuprate superconductors arise from this renormalization of the electrons.

Among the unusual features that are unique to the cuprate superconductors, in addition to the exceptionally strong superconductivity, the normal-state pseudogap is perhaps the most noteworthy, however, the origin of the normal-state pseudogap remains a subject of debate. During the last over three decades, several scenarios were proposed to explain the formation of the normal-state pseudogap. In particular, it has been argued⁷⁸ that the normal-state pseudogap originates from preformed pairs at T^* , which would then condense (that is, become phase coherent) at T_c . On the other hand, it has been suggested that the normal-state pseudogap is distinct from the SC gap and related with a certain order which competes with superconductivity⁷⁹. Moreover, it has been proposed that the normal-state pseudogap is a combination of a quantum disordered d-wave superconductor and an entirely different form of competing order, originating from the particle-hole channel⁸⁰. In the present framework of the kinetic-energy-driven superconductivity, the normal-state pseudogap is intimately connected to the electron normal self-energy. To see this intimate connection more clearly, the above electron normal self-energy in Eq. (5a) can be also rewritten as,

$$\Sigma_{\text{ph}}(\mathbf{k}, \omega) \approx \frac{[2\bar{\Delta}_{\text{PG}}(\mathbf{k})]^2}{\omega - \varepsilon_{\mathbf{k}}}, \quad (6)$$

and then the momentum-dependent normal-state pseudogap $\bar{\Delta}_{\text{PG}}(\mathbf{k})$ is obtained straightforwardly as,

$$\bar{\Delta}_{\text{PG}}^2(\mathbf{k}) = -\frac{1}{4}\varepsilon_{\mathbf{k}}\Sigma_{\text{ph}}(\mathbf{k}, 0), \quad (7)$$

with the normal-state pseudogap parameter $\bar{\Delta}_{\text{PG}}^2 = (1/N)\sum_{\mathbf{k}}\bar{\Delta}_{\text{PG}}^2(\mathbf{k})$. This momentum-dependent normal-state pseudogap is identified as being a region of the electron normal self-energy in which the normal-state pseudogap anisotropically suppresses the electronic density of states on EFS. In particular, the present results also show that the same interaction between electrons mediated by the spin excitation that is responsible for pairing the electrons in the particle-particle channel also generates the normal-state pseudogap state in the particle-hole channel^{72,73}. Moreover, it should be noted that in spite of the origins of the formation of the normal-state pseudogap, the main feature of the full electron propagators in Eq. (3) together with the SC gap $\bar{\Delta}_{\mathbf{k}}$ and the electron normal self-energy (then the normal-state pseudogap) in Eq. (6) are similar to those proposed from several phenomenological theories⁸⁰⁻⁸⁴ of the normal-state pseudogap-state based on the d-wave BCS formalism, where a phenomenological normal-state pseudogap is introduced to describe the two-gap feature in cuprate superconductors.

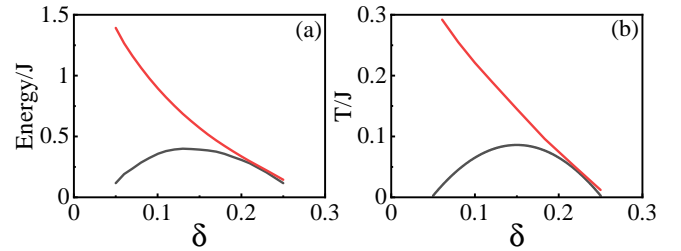


FIG. 1: (Color online) (a) The electron pair gap $2\bar{\Delta}$ (black-line) and normal-state pseudogap $2\bar{\Delta}_{\text{PG}}$ (red-line) as a function of doping with temperature $T = 0.002J$. (b) The superconducting transition temperature T_c (black-line) and the normal-state pseudogap crossover temperature T^* (red-line) as a function of doping.

For a better understanding of the interplay between the SC-state and normal-state pseudogap-state in the cuprate superconductors, we have performed a series of calculations for the electron pair gap parameter $\bar{\Delta}$ and normal-state pseudogap parameter $\bar{\Delta}_{\text{PG}}$ at different doping levels [see Appendix A], and the results of $2\bar{\Delta}$ (black-line) and $2\bar{\Delta}_{\text{PG}}$ (red-line) as a function of doping with temperature $T = 0.002J$ are plotted in Fig. 1a. Apparently, the exotic two-gap feature detected from the cuprate superconductors⁸ is qualitatively reproduced, where with the increase of doping, the electron pair gap $\bar{\Delta}$ is raised monotonically in the underdoped regime, and reaches its maximum at around the optimal doping $\delta \approx 0.15$. However, with the further increase of doping, $\bar{\Delta}$ then turns into a gradual decrease in the overdoped regime. On the other hand, in contrast to the case of $\bar{\Delta}$ in the underdoped regime, the normal-state pseudogap $\bar{\Delta}_{\text{PG}}$ in the underdoped regime is much larger than $\bar{\Delta}$ in the underdoped regime, reflecting a basic experimental fact that the normal-state pseudogap-state is particularly obvious in the underdoped regime. This normal-state pseudogap $\bar{\Delta}_{\text{PG}}$ smoothly decreases with the increase of doping. In particular, $\bar{\Delta}_{\text{PG}}$ seems to merge with $\bar{\Delta}$ in the strongly overdoped region, eventually going to zero together with $\bar{\Delta}$ at the end of the SC dome.

Both the above electron pair gap and normal-state pseudogap are strong temperature dependent. In particular, in a given doping concentration, the electron pair gap vanishes at T_c , while the normal-state pseudogap disappears when temperature reaches the normal-state pseudogap crossover temperature T^* . To see the different doping-dependent trends of T_c and T^* in the underdoped regime more clearly, we have also made a series of calculations for T_c and T^* at different doping concentrations [see Appendix A], and the results of T_c (black-line) and T^* (red-line) as a function of doping are plotted in Fig. 1b, where in conformity with the doping dependence of $\bar{\Delta}$ and $\bar{\Delta}_{\text{PG}}$ shown in Fig. 1a, (i) T_c increases with the increase of doping in the underdoped regime, and reaches its maximum at around the optimal doping, then decreases in the overdoped regime⁷³; (ii) T^* is much larger than T_c in the underdoped regime, then

it smoothly decreases with the increase of doping, eventually terminating together with T_c at the end of the SC dome, in qualitative agreement with the experimental observations⁸. This normal-state pseudogap crossover temperature T^* is actually a crossover line below which a novel electronic state emerges, as exemplified by the presence of the disconnected Fermi arcs, the competing electronic orders, the PDH structure in the energy distribution curve, etc., and then the anomalous properties correlated to the formation of the normal-state pseudogap discussed in the next Sec. III are explained in a natural way.

III. QUANTITATIVE CHARACTERISTICS OF LOW-ENERGY ELECTRONIC STRUCTURE

In this section, we discuss the quantitative characteristics of the low-energy electronic structure in the underdoped cuprate superconductors, and show how the normal-state pseudogap leads to the crucial effect on the redistribution of the spectral weight on EFS, the energy distribution curves, and the ARPES autocorrelation.

The anomalous properties of the electronic structure observed from ARPES experiments can be analyzed theoretically in terms of the ARPES spectral intensity^{10–12},

$$I(\mathbf{k}, \omega) \propto n_F(\omega) A(\mathbf{k}, \omega), \quad (8)$$

with the fermion distribution $n_F(\omega)$ and the electron spectral function,

$$A(\mathbf{k}, \omega) = \frac{1}{\pi} \frac{\tilde{\Gamma}_{\mathbf{k}}(\omega)}{[\omega - \varpi_{\mathbf{k}}(\omega)]^2 + [\tilde{\Gamma}_{\mathbf{k}}(\omega)]^2}, \quad (9)$$

where the quasiparticle energy dispersion $\varpi_{\mathbf{k}}(\omega)$ and quasiparticle scattering rate $\tilde{\Gamma}_{\mathbf{k}}(\omega)$ in the SC-state can be expressed explicitly as,

$$\varpi_{\mathbf{k}}(\omega) = \varepsilon_{\mathbf{k}} - \text{Re}\Sigma_{\text{tot}}(\mathbf{k}, \omega), \quad (10a)$$

$$\tilde{\Gamma}_{\mathbf{k}}(\omega) = \text{Im}\Sigma_{\text{tot}}(\mathbf{k}, \omega), \quad (10b)$$

with $\text{Re}\Sigma_{\text{tot}}(\mathbf{k}, \omega)$ and $\text{Im}\Sigma_{\text{tot}}(\mathbf{k}, \omega)$ that are respectively the real and imaginary parts of the electron total self-energy $\Sigma_{\text{tot}}(\mathbf{k}, \omega)$. The above results in Eq. (10) show that the constrained electrons in the cuprate superconductors are renormalized to form the quasiparticles due to the electron scattering mediated by the spin excitation and therefore they acquire a finite lifetime.

A. Electron Fermi surface reconstruction

EFS is usually defined in the normal-state, which separates the filled electronic states from the empty electronic states, and therefore plays a key role in the understanding of the anomalous properties in the cuprate superconductors. Experimentally, the *intensity map* of the ARPES

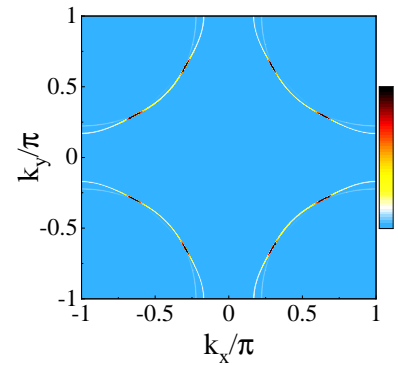


FIG. 2: (Color online) The intensity map of the normal-state ARPES spectrum in $[k_x, k_y]$ plane for the zero binding-energy $\omega = 0$ at $\delta = 0.10$ with $T = 0.002J$.

spectrum at the zero energy is often adopted to measure the underlying EFS^{10–12}, i.e., the underlying EFS is determined by measuring the ARPES spectrum at the zero energy to map out the locus of the maximum in the intensity.

In the normal-state ($\bar{\Delta} = 0$), the quasiparticle energy dispersion and quasiparticle scattering rate in Eq. (10) in the SC-state are respectively reduced as,

$$\varpi_{\mathbf{k}}(\omega) = \varepsilon_{\mathbf{k}} - \text{Re}\Sigma_{\text{ph}}(\mathbf{k}, \omega), \quad (11a)$$

$$\tilde{\Gamma}_{\mathbf{k}}(\omega) = \text{Im}\Sigma_{\text{ph}}(\mathbf{k}, \omega) \approx \pi[2\bar{\Delta}_{\text{PG}}(\mathbf{k})]^2 \delta(\omega - \varepsilon_{\mathbf{k}}), \quad (11b)$$

where $\text{Re}\Sigma_{\text{ph}}(\mathbf{k}, \omega)$ and $\text{Im}\Sigma_{\text{ph}}(\mathbf{k}, \omega)$ are the real and imaginary parts of the electron normal self-energy $\Sigma_{\text{ph}}(\mathbf{k}, \omega)$, respectively. The result in Eq. (11b) thus indicates directly that there is an intrinsic link between the quasiparticle scattering rate and normal-state pseudogap, in agreement with the ARPES experimental observations⁸⁵. In this case, the location of the EFS contour in momentum space is determined directly by,

$$\varepsilon_{\mathbf{k}} + \text{Re}\Sigma_{\text{ph}}(\mathbf{k}, 0) = 0, \quad (12)$$

from Eq. (11a), and then the lifetime of the quasiparticles on the EFS contour is governed by the inverse of the quasiparticle scattering rate $\tilde{\Gamma}_{\mathbf{k}}(0)$ [then the normal-state pseudogap $\bar{\Delta}_{\text{PG}}(\mathbf{k})$ in Eq. (11b)]. In other words, the EFS contour is determined by the poles of the electron propagator at zero energy in Eq. (11a), while the redistribution of the spectral weight on the EFS contour is mainly dominated by the quasiparticle scattering rate $\tilde{\Gamma}_{\mathbf{k}}(0)$ [then the normal-state pseudogap $\bar{\Delta}_{\text{PG}}(\mathbf{k})$ in Eq. (11b)]. In Fig. 2, we plot the intensity map of the ARPES spectrum in the normal-state for the zero binding-energy $\omega = 0$ at $\delta = 0.10$ with $T = 0.002J$. It thus shows clearly that the spectral weight redistributes along with the EFS contour due to the opening of the momentum-dependent normal-state pseudogap, where the most exotic features can be summarized as^{46,73}: (a) at around the antinodal region, the normal-state pseudogap suppresses strongly the spectral weight, which leads to that the EFS contour at around the antinodal region becomes unobservable in

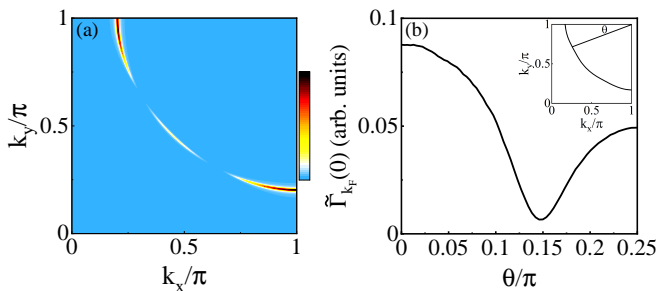


FIG. 3: (a) The intensity map of the normal-state quasiparticle scattering rate in the $[k_x, k_y]$ plane and (b) the angular dependence of the normal-state quasiparticle scattering rate along \mathbf{k}_F from the antinode to the node for the binding-energy $\omega = 0$ at $\delta = 0.10$ with $T = 0.002J$.

experiments¹⁷⁻²⁵; (b) at around the nodal region, the normal-state pseudogap suppresses modestly the spectral weight, which leads to that the EFS contour is broken up into four disconnected Fermi arcs located at around the nodal region¹⁷⁻²⁵; (c) at around the tips of the Fermi arcs, the renormalization from the quasiparticle scattering further reduces the most of the spectral weight on the Fermi arcs to the tips of the Fermi arcs²¹⁻²⁵, indicating that the quasiparticles at around the tips of the disconnected Fermi arcs have the largest density of states, and then these quasiparticles at around the tips of the Fermi arcs contribute effectively to the quasiparticle scattering process. It should be noted that the result of the intensity map of the ARPES spectrum in Fig. 2 is qualitatively consistent with some ARPES observations²¹⁻²⁵, where the sharp quasiparticle peak with large spectral weight appears always at off-node place. On the other hand, the ARPES observations⁴¹ also indicate that the highest intensity points in the intensity map of the ARPES spectrum for a *finite binding-energy* are located exactly at the tips of the Fermi arcs.

Since the redistribution of the spectral weight on the EFS contour is mainly dominated by the quasiparticle scattering rate $\tilde{\Gamma}_{\mathbf{k}}(0)$ [then the normal-state pseudogap $\tilde{\Delta}_{\text{PG}}(\mathbf{k})$] in Eq. (11b) as mentioned above, the formation of four disconnected Fermi arcs due to the EFS reconstruction is directly linked with the opening of the highly anisotropic momentum-dependence of the normal-state pseudogap^{46,73,85}. To see this picture more clearly, we have made a series of the calculations for the quasiparticle scattering rate $\tilde{\Gamma}_{\mathbf{k}_F}(0) = \text{Im}\Sigma_{\text{ph}}(\mathbf{k}_F, 0)$ in the normal-state, and the result of the intensity map of $\tilde{\Gamma}_{\mathbf{k}_F}(0)$ in the $[k_x, k_y]$ plane for the zero binding-energy $\omega = 0$ at $\delta = 0.10$ with $T = 0.002J$ is plotted in Fig. 3a. Apparently, $\tilde{\Gamma}_{\mathbf{k}_F}(0)$ is strong dependence of momentum, reflecting a fact that the anisotropic $\tilde{\Gamma}_{\mathbf{k}_F}(0)$ [then the normal-state pseudogap $\tilde{\Delta}_{\text{PG}}(\mathbf{k}_F)$] in momentum-space is strongly non-monotonous angle dependent. To illuminate this fact more clearly, we plot the angular dependence of $\tilde{\Gamma}_{\mathbf{k}_F}(0)$ along the EFS contour from the antinode to the node for the zero binding-energy $\omega = 0$ at

$\delta = 0.10$ with $T = 0.002J$ in Fig. 3b, where the actual minimum of $\tilde{\Gamma}_{\mathbf{k}_F}(0)$ always appears at the off-node place, and is accommodated exactly at the tip of the disconnected Fermi arc. In particular, the largest magnitude of $\tilde{\Gamma}_{\mathbf{k}_F}(0)$ appears at the antinode, which is consistent with the experimental observations²¹⁻²⁸, where the strongest quasiparticle scattering appeared at the antinodes has been also observed. However, the magnitude of $\tilde{\Gamma}_{\mathbf{k}_F}(0)$ decreases with the shift of the momentum away from the antinode, leading to that the magnitude of $\tilde{\Gamma}_{\mathbf{k}_F}(0)$ at around the nodal region is always less than that at around the antinodal region. This highly anisotropic momentum-dependence of the quasiparticle scattering rate $\tilde{\Gamma}_{\mathbf{k}_F}(0)$ [then the normal-state pseudogap $\tilde{\Delta}_{\text{PG}}(\mathbf{k}_F)$] thus reduces strongly the spectral weight on the EFS contour at around the antinodal region, but it has a more modest effect on the spectral weight on the EFS contour at around the nodal region, and then the most of the spectral weight on the EFS contour sites at around the tips of the disconnected Fermi arcs. This special momentum dependence of $\tilde{\Gamma}_{\mathbf{k}_F}(0)$ [then the normal-state pseudogap $\tilde{\Delta}_{\text{PG}}(\mathbf{k}_F)$] leads to that the density of states of the quasiparticles at around the nodal region is higher than that at around the antinodal region, and therefore generates the formation of four disconnected Fermi arcs with the largest density of states of the quasiparticles located at around the tips of the disconnected Fermi arcs.

In the past several years, some experimental observations have indicated clearly that the charge-order state emerges just below the normal-state pseudogap crossover temperature T^* , with a characteristic charge-order wave vector that matches well with the tips on the straight Fermi arcs²⁵⁻²⁹. Moreover, these experimental observations also show that the charge-order state is particularly obvious in the underdoped regime, and then the magnitude of the charge-order wave vector Q_{CO} smoothly decreases with the increase of doping²⁵⁻²⁹. In the present study, we find that the theoretical result of the quasiparticle scattering wave vector between the tips on the straight Fermi arcs shown in Fig. 2 at $\delta = 0.10$ is $Q_{\text{CO}} = 0.295$ (here we use the reciprocal units), which is in qualitative agreement with the experimental average value²⁵⁻²⁹ of the charge-order wave vector $Q_{\text{CO}} \approx 0.265$ observed in the underdoped pseudogap phase. The charge-order state is characterized by the charge-order wave vector, and the qualitative agreement between theory and experiments in the charge-order wave vector therefore is important to confirm that the charge-order state is driven by the EFS instability⁴⁶. In particular, the decrease of the normal-state pseudogap with the increase of doping shown in Fig. 1a also leads to that the charge-order wave vector decreases with the increase of doping⁴⁶, also in qualitative agreement with the experimental observations²⁵⁻²⁹. Moreover, this charge-order correlation developed in the normal-state pseudogap phase can persists into the SC-state, leading to a coexistence of charge order and superconductivity below

T_c . The above results therefore indicate that the charge-order state is manifested within the normal-state pseudogap phase, then the formation of the disconnected Fermi arcs, the charge-order state, and the normal-state pseudogap in the underdoped cuprate superconductors are intimately related to each other, and they have a root in common originated from the interaction between electrons by the exchange of the spin excitation.

B. Line-shape in energy distribution curve

We now turn to discuss the complicated line-shape in the energy distribution curve of the underdoped cuprate superconductors. One of the most remarkable features in the energy distribution curve of the underdoped cuprate superconductors observed from ARPES experiments has been the PDH structure, where a very sharp peak appears at the low binding-energy, followed by a dip and then a hump in the higher binding-energy, leading to the formation of a PDH structure^{31–40}. This striking PDH structure was found firstly in $\text{Bi}_2\text{Sr}_2\text{CaCu}_2\text{O}_{8+\delta}$ at around the antinodal region^{31,32}. Later, this outstanding PDH structure was also observed in other families of cuprate superconductors^{33–36}, and now is a hallmark of the spectral line-shape of the energy distribution curves in the underdoped cuprate superconductors. After intensive studies for about four decades, although it is believed widely that the appearance of the *dip* in the energy distribution curves is due to the very strong scattering of the electrons by a *particular bosonic excitation*, the nature of this bosonic excitation remains controversial, where two main proposals are disputing the explanations of the origin of the dip^{31–40}: in one of the proposals, the dip is associated with the strong electron-phonon coupling, while in the other, the dip is related to the pseudogap originating from the spin excitation. In this subsection, we show clearly that the complicated line-shape in the energy distribution curves is affected strongly by the normal-state pseudogap, and then the dip in the energy distribution curves associated with the renormalization of the electrons is electronic in nature^{47,86,87}.

In Fig. 4a, we plot the energy distribution curve at the antinode in the SC-state as a function of binding-energy for $\delta = 0.10$ with $T = 0.002J$, where the energy distribution curve consists of two distinct peaks: a very sharp low-energy peak and a relatively broad high-energy peak. The high-energy peak is corresponding to the hump, and the low-energy peak is corresponding to the SC quasiparticle excitation, while the deviation of the low-energy peak from EFS is due to the opening of the d-wave type SC gap. A spectral dip is located between these two distinct peaks, which is corresponding to the intensity depletion region. The total contributions for the energy distribution curve thus lead to the formation of the PDH structure, in qualitative agreement with the ARPES experimental observations on cuprate superconductors^{31–40}. However, this exotic PDH struc-

ture is also observed experimentally in the underdoped pseudogap phase^{32,38}. To see this point more clearly, the

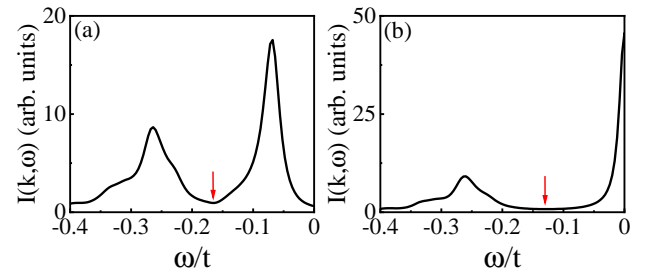


FIG. 4: The energy distribution $\tilde{\Gamma}_{\mathbf{k}}(\omega)$ curve at the antinode (a) in the superconducting-state and (b) in the normal-state as a function of binding-energy for $\delta = 0.10$ with $T = 0.002J$. The red arrow indicating the position of the dip at the dip energy ω_{dip} .

energy distribution curve at the antinode in the normal-state as a function of binding-energy for $\delta = 0.10$ with $T = 0.002J$ is also plotted in Fig. 4b. Comparing it with Fig. 4a for the same set of parameters except for $\Delta = 0$, we see that (i) the overall feature of the line-shape in the energy distribution curve in the normal-state presents a similar behavior of the line-shape in the SC-state; (ii) however, in a difference to the case in the SC-state, the sharp low-energy peak is shifted to EFS in the normal-state due to the disappearance of the SC gap, also in qualitative agreement with the ARPES experimental observations^{32,38}.

In the energy distribution curve^{10–12}, a quasiparticle with a long lifetime is observed as a sharp peak in intensity, and a quasiparticle with a short lifetime is observed as a broad hump, while the dip in the energy distribution curve implies that the quasiparticle scattering rate has a sharp peak accommodated at around the dip energy^{40,47,86,87}. This can be well understood from the quasiparticle energy dispersion $\varpi_{\mathbf{k}}(\omega)$ in Eq. (10a) and quasiparticle scattering rate $\tilde{\Gamma}_{\mathbf{k}}(\omega)$ in Eq. (10b). The ARPES spectrum exhibits a peak when the incoming photon energy ω is equal to the quasiparticle excitation energy $\varpi_{\mathbf{k}}(\omega)$, i.e.,

$$\omega - \varpi_{\mathbf{k}}(\omega) = \omega - \varepsilon_{\mathbf{k}} - \text{Re}\Sigma_{\text{tot}}(\mathbf{k}, \omega) = 0, \quad (13)$$

and then the width of this peak at the energy ω is dominated by the quasiparticle scattering rate $\tilde{\Gamma}_{\mathbf{k}}(\omega)$ [then the normal-state pseudogap $\Delta_{\text{PG}}(\mathbf{k})$]. In Fig. 5a, we plot $\tilde{\Gamma}_{\mathbf{k}}(\omega)$ at the antinode in the SC-state as a function of binding-energy for $\delta = 0.10$ with $T = 0.002J$. For a clear comparison, the experimental result⁴⁰ detected in $\text{Bi}_2\text{Sr}_2\text{CaCu}_2\text{O}_{8+\delta}$ in the SC-state is also shown in Fig. 5b. The present result in Fig. 5a shows that $\tilde{\Gamma}_{\mathbf{k}}(\omega)$ has a well-pronounced peak structure^{47,86,87}, where $\tilde{\Gamma}_{\mathbf{k}}(\omega)$ exhibits a sharp peak at the binding-energy ω_{dip} , and then the weight of this sharp peak reduces rapidly away from the peak, which is well consistent with the experimental results⁴⁰. In particular, the position of this sharp peak

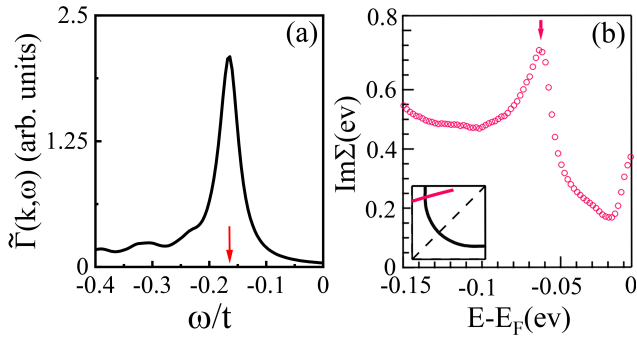


FIG. 5: (a) The quasiparticle scattering rate at the antinode in the superconducting-state as a function of binding-energy for $\delta = 0.10$ with $T = 0.002J$. (b) The experimental result of $\text{Bi}_2\text{Sr}_2\text{CaCu}_2\text{O}_{8+\delta}$ taken from Ref. 40.

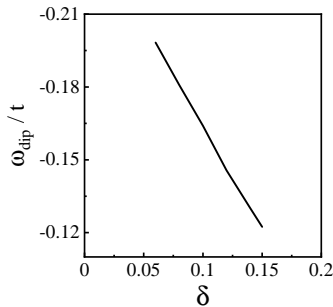


FIG. 6: The antinodal dip energy ω_{dip} in the superconducting-state as function of doping with $T = 0.002J$.

in $\tilde{\Gamma}_{\mathbf{k}}(\omega)$ is just corresponding to the position of the dip in the PDH structure shown in Fig. 4b, which therefore confirms that the intensity depletion in the energy distribution curve at around the dip is a natural consequence of the peak structure in $\tilde{\Gamma}_{\mathbf{k}}(\omega)$. Moreover, the dip in the energy distribution curve is shifted towards to EFS when the doping is increased in the underdoped regime. To see this point more clearly, we plot the dip energy ω_{dip} in the SC-state as a function of doping with $T = 0.002J$ in Fig. 6, where ω_{dip} as a function of doping in the underdoped regime presents a similar behavior of the normal-state pseudogap $\tilde{\Delta}_{\text{PG}}$ shown in Fig. 1a, also in qualitative agreement with the experimental observations^{31–40}. This SC-state coexists with the normal-state pseudogap below T_c . In this case, as a comparison, we have also calculated the quasiparticle scattering rate $\tilde{\Gamma}_{\mathbf{k}}(\omega)$ at the antinode in the normal-state pseudogap phase as a function of binding-energy for the same set of parameters as in Fig. 5a, and the obtained result shows that the overall feature of the quasiparticle scattering rate in the normal-state pseudogap phase is almost the same as that in the SC-state shown in Fig. 5a, and then the peak structure in the quasiparticle scattering rate leads to the formation of a similar PDH structure in the energy distribution curve in the normal-state pseudogap phase as shown in Fig. 4a. The above results therefore also show that the well-known PDH structure in the energy distribution curve

can be attributed to the emergence of the normal-state pseudogap.

C. ARPES autocorrelation

The ARPES autocorrelation^{41–43},

$$\bar{C}(\mathbf{q}, \omega) = \frac{1}{N} \sum_{\mathbf{k}} I(\mathbf{k} + \mathbf{q}, \omega) I(\mathbf{k}, \omega), \quad (14)$$

can be analyzed in terms of the ARPES spectrum (8), where the summation of momentum \mathbf{k} is restricted within the first Brillouin zone (BZ). This ARPES autocorrelation therefore detects the autocorrelation of the ARPES spectra at two different momenta \mathbf{k} and $\mathbf{k} + \mathbf{q}$ with a fixed energy ω . Experimentally, the ARPES spectrum reveals straightforwardly the momentum-space electronic structure^{10–12}, while the ARPES autocorrelation spectrum reveals straightforwardly the effectively momentum-resolved joint density of states in the electronic state^{41–43}, and then both the spectra yield the important insights into the nature of the electronic state. More importantly, the experimental observations have provided the unambiguous evidence^{41–43} that the sharp peaks in the ARPES autocorrelation spectrum in the SC-state are directly linked to the quasiparticle scattering wave vectors \mathbf{q}_i connecting the tips of the Fermi arcs obeying an octet scattering model, and are also well consistent with the quasiparticle scattering interference peaks observed from the Fourier transform STS experiments^{88–96}. However, although the experimental data of the ARPES autocorrelation spectrum in the SC-state have been available^{41–43}, the experimental data of the ARPES autocorrelation spectrum in the normal-state pseudogap phase are still lacking to date. In this subsection, we further discuss the influence of the pseudogap on the electronic state of the underdoped cuprate superconductors in terms of the ARPES autocorrelation.

In subsection III A, the intensity map of the normal-state ARPES spectrum at the zero binding-energy has been discussed⁴⁶, where the redistribution of the spectral weight on EFS leads to the formation of the disconnected Fermi arcs. However, this spectral weight redistribution shown in Fig. 2 at the case for the zero binding-energy can persist into the system at the case for a finite binding-energy⁴⁸. For a convenience in the following discussions of the unusual features of the ARPES autocorrelation, we firstly discuss the essential properties of the constant energy contour at the case for a finite binding-energy. In Fig. 7a, we plot an intensity map of the SC-state ARPES spectrum $I(\mathbf{k}, \omega)$ in Eq. (8) for the binding-energy $\omega = 0.12J$ at $\delta = 0.10$ with $T = 0.002J$. For a clear comparison, the ARPES experimental data⁴¹ detected from $\text{Bi}_2\text{Sr}_2\text{CaCu}_2\text{O}_{8+\delta}$ in the SC-state for the binding-energy $\omega = 12$ meV is also shown in Fig. 7b. As in the case of the spectral weight redistribution shown in Fig. 2, (i) the formation of the disconnected Fermi

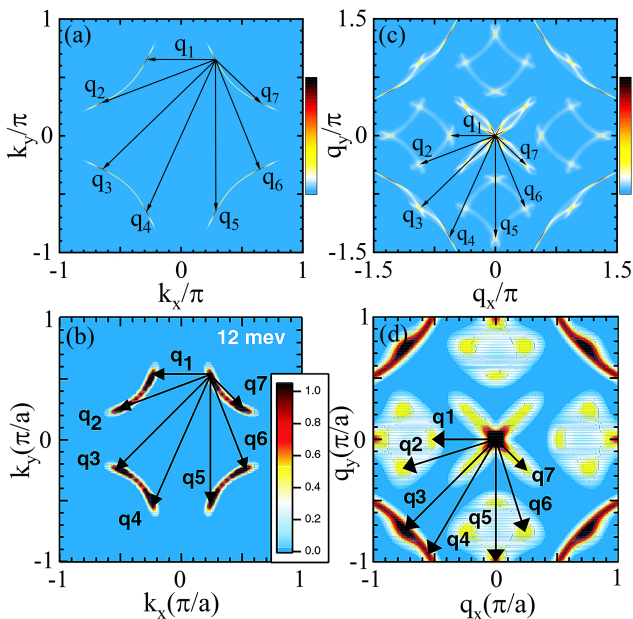


FIG. 7: (Color online) (a) The intensity map of the ARPES spectrum in the superconducting-state for the binding-energy $\omega = 0.12J$ at $\delta = 0.10$ with $T = 0.002J$. (b) The experimental result observed on $\text{Bi}_2\text{Sr}_2\text{CaCu}_2\text{O}_{8+\delta}$ for the binding-energy $\omega = 12$ meV taken from Ref. 41. (c) The intensity map of the ARPES autocorrelation in the superconducting-state for the binding-energy $\omega = 0.12J$ at $\delta = 0.10$ with $T = 0.002J$. (d) The experimental result observed from $\text{Bi}_2\text{Sr}_2\text{CaCu}_2\text{O}_{8+\delta}$ for the binding-energy $\omega = 12$ meV taken from Ref. 41. The eight tips of the disconnected Fermi arcs determine the scattering wave vectors within the octet scattering model, while the scattering wave vectors which connect these tips of the disconnected Fermi arcs are shown as arrows labeled by the designation of each scattering wave vector \mathbf{q}_i .

arcs on EFS induced by the normal-state pseudogap persists into the case of the constant energy contour for a finite binding-energy⁴⁸, where the notation *Fermi arcs* on the constant energy contour has been used even for a finite binding-energy⁴¹; (ii) the points with the highest intensity do not accommodate at around the nodes, but they locate exactly at around the tips of the disconnected Fermi arcs; (iii) these tips of the disconnected Fermi arcs connected by the scattering wave vectors \mathbf{q}_i construct an *octet scattering model*, which is well consistent with the corresponding ARPES experimental observations^{41–43}.

We are now ready to discuss the ARPES autocorrelation in the underdoped cuprate superconductors. In Fig. 7c, we plot the intensity map of the ARPES autocorrelation $\bar{C}(\mathbf{q}, \omega)$ in the SC-state for the binding-energy $\omega = 0.12J$ at $\delta = 0.10$ with $T = 0.002J$ in comparison with (d) the experimental result⁴¹ of the intensity map of the ARPES autocorrelation detected from $\text{Bi}_2\text{Sr}_2\text{CaCu}_2\text{O}_{8+\delta}$ in the SC-state for the binding-energy $\omega = 12$ meV. The result in Fig. 7c thus shows that some sharp peaks appear in the ARPES autocorrelation pattern, where the joint density of states is highest⁴⁸. More

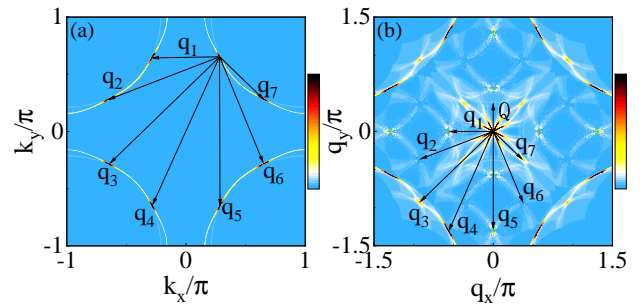


FIG. 8: (Color online) (a) The intensity map of the ARPES spectrum in the normal-state for the binding-energy $\omega = 12$ meV at $\delta = 0.10$ with $T = 0.002J$. (b) The intensity map of the ARPES autocorrelation in the normal-state for the binding-energy $\omega = 0.12J$ at $\delta = 0.10$ with $T = 0.002J$. As the case of the superconducting-state shown in Fig. 7, the scattering wave vectors \mathbf{q}_i in the normal-state also obey the octet scattering model, while \mathbf{Q} in (b) indicates the checkerboard scattering wave vector.

specifically, these sharp peaks in the ARPES autocorrelation pattern are straightforwardly correlated with the wave vectors \mathbf{q}_i connecting the tips of the disconnected Fermi arcs on the constant energy contour shown in Fig. 7a, which are well consistent with the ARPES experimental observations^{41–43}. The above results in Fig. 7 thus also confirm that in the SC-state, the *octet scattering model* constructed by the eight tips of the disconnected Fermi arcs can give a consistent description of the regions of the highest joint density of states in the ARPES autocorrelation spectrum⁴⁸.

Although the SC-state of the underdoped cuprate superconductors coexists and competes with the normal-state pseudogap state, the quasiparticle still exhibits the particle-hole mixing similar to that in the conventional superconductors^{10–12}. In particular, in the low-energy limit, the quasiparticle energy dispersion $\varpi_{\mathbf{k}}(\omega)$ in Eq. (10a) in the SC-state can be reduced as [see Appendix A], $\varpi_{\mathbf{k}} = E_{\mathbf{k}}$, where $E_{\mathbf{k}} = \sqrt{\bar{\varepsilon}_{\mathbf{k}}^2 + |\bar{\Delta}_{Z\mathbf{k}}|^2}$, with $\bar{\varepsilon}_{\mathbf{k}} = Z_F \varepsilon_{\mathbf{k}}$, and $\bar{\Delta}_{Z\mathbf{k}} = Z_F \bar{\Delta}_{\mathbf{k}}$, while the single-particle coherent weight Z_F that is directly associated with the normal-state pseudogap has been given explicitly in Appendix A. In this case, the scattering wave vector \mathbf{q}_i dominates the ARPES autocorrelation at energy ω , since these \mathbf{k} -pairs on the constant energy contour shown in Fig. 7a connected by the wave vector \mathbf{q}_i have a high joint density of states. This also follows from a basic fact that the magnitude of the SC gap $|\bar{\Delta}_{\mathbf{k}}|$ is \mathbf{k} -dependent, and then some different minima ω_i , at which the quasiparticles emerge, occur at the tips of the disconnected Fermi arcs^{88,89}. On the other hand, the square-lattice CuO_2 plane has a four-fold symmetry, this implies that at any non-zero energy ω_i , there are only eight possible \mathbf{k}_F values at which $|\bar{\Delta}_{Z\mathbf{k}}| = \omega_i$ in the first BZ^{88,89}. The highest joint density of states for the quasiparticle scattering at this energy ω_i occur at \mathbf{q}_i -vectors connecting

the eight tips of the Fermi arcs. This is why the sharp peaks in the ARPES autocorrelation occur at these \mathbf{q}_i -vectors. However, in the normal-state pseudogap phase, where the SC gap $\bar{\Delta} = 0$, the additional distinct peaks (then the additional distinct electronic orders) in the ARPES autocorrelation spectrum that are suppressed strongly by the SC gap appear. To understand the nature of these additional distinct peaks in the ARPES autocorrelation spectrum in the normal-state more clearly, we plot (a) the intensity map of the ARPES spectrum $I(\mathbf{k}, \omega)$ in the normal-state and (b) the intensity map of the ARPES autocorrelation $\bar{C}(\mathbf{q}, \omega)$ in the normal-state for the binding-energy $\omega = 12$ meV at $\delta = 0.10$ with $T = 0.002J$ in Fig. 8. In a careful comparison with the corresponding results in the SC-state shown in Fig. 7, the similarities and differences of the ARPES autocorrelation patterns between the SC- and normal-states can be summarized as: (i) the overall features of the redistribution of the spectral weight on the constant-energy-contour for a finite binding-energy in the SC-state persist into the case in the normal-state for a finite binding-energy, indicating that the redistribution of the spectral weight on the constant-energy-contour is mainly dominated by the normal-state pseudogap; (ii) the overall features of the ARPES autocorrelation peaks labelled by \mathbf{q}_i ($i = 1, \dots, 7$) in the normal-state are well consistent with those in the SC-state, reflecting an experimental fact that the multiple electronic order-states that emerge in the normal-state above T_c persist into the SC-state below T_c , and then they coexist and compete with the SC-state. In particular, the quasiparticle scattering between two tips of the straight Fermi arcs with the scattering wave vector $\mathbf{q}_1 = \mathbf{Q}_{CO}$ matches well with the corresponding charge-order wave vector found in the resonant X-ray scattering measurements and STS experiments²⁵⁻³⁰, which thus confirms the charge-order state is driven by the EFS instability^{25-29,46}; (iii) however, the additional distinct peaks along the parallel direction that are suppressed strongly by the SC-gap emerge, leading to the formation of the *checkerboard* peaks (then the *checkerboard charge ordering*), with the scattering wave vectors of $\mathbf{Q} \approx [\pm 0.38\pi, 0]$ and $\mathbf{Q} \approx [0, \pm 0.38\pi]$. In particular, it should be noted that although the experimental data of the checkerboard charge ordering in the underdoped pseudogap phase observed directly from the ARPES autocorrelation are still lacking to date, the early ARPES experiments⁹⁷ have observed the *checkerboard charge ordering* in the underdoped pseudogap phase above T_c . Moreover, by virtue of systematic studies using the STS measurements⁹⁸, the electronic checkerboard patterns have been detected directly in the underdoped pseudogap phase above T_c . On the other hand, some STS experimental measurements⁹⁹⁻¹⁰¹ also indicate that although the electronic checkerboard ordering appeared in the underdoped pseudogap phase can persist into the SC-state below T_c , the magnitude of the incoming photon energy in these experiments is much larger than that of the SC gap ($|\omega| > \bar{\Delta}$). However, whether the checkerboard

charge ordering observed in the normal-state pseudogap phase or observed in the SC-state with $|\omega| > \bar{\Delta}$, the average values of the checkerboard charge-order wave vectors have been identified in these experiments^{88,89,97-101} as $\mathbf{Q} \approx [\pm 0.44\pi, 0] \pm 15\%$ and $\mathbf{Q} \approx [0, \pm 0.44\pi] \pm 15\%$, which are qualitatively consistent with the present results.

Since all the features observed in the STS experiments, both in the SC-state and in the pseudogap phase, are related to the momentum-space profiles of the joint density of states¹⁰², we¹⁰³ have started very recently from the homogeneous electron propagator in Eq. (3) to study the local density of states (LDOS) modulation in the underdoped cuprate superconductors within the T -matrix approach, where LDOS is derived for various kinds of impurities, and the obtained results show that the pronounced peaks in the momentum-space LDOS modulation pattern are qualitatively consistent with the present results of the ARPES autocorrelation patterns shown in Fig. 7 and Fig. 8. These and the related results will be presented elsewhere.

IV. SUMMARY

Within the framework of the kinetic-energy-driven superconductivity, we have studied the effect of the normal-state pseudogap on the low-energy electronic structure in the underdoped cuprate superconductors. Our results show that the interaction between electrons directly from the kinetic energy by the exchange of the spin excitation generates the normal-state pseudogap-state in the particle-hole channel and the SC-state in the particle-particle channel, where the normal-state pseudogap and the SC gap respectively originate from the electron normal self-energy in the particle-hole channel and the electron anomalous self-energy in the particle-particle channel, and are derived explicitly by taking into account the vertex correction. This normal-state pseudogap-state coexists and competes with the SC-state below T_c , which leads to that T_c is raised gradually with the increase of doping in the underdoped regime, and then achieves its maximum at around the optimal doping, subsequently, T_c decreases monotonically with the increase of doping in the overdoped regime. However, in a striking contrast to T_c in the underdoped regime, T^* is much higher than T_c in the underdoped regime, then it smoothly decreases when the doping is increased, and both T^* and T_c converge to the end of the SC dome. Concomitantly, a number of the exotic features of the low-energy electronic structure are directly correlated to the opening of the normal-state pseudogap: (i) the redistribution of the spectral weight on the EFS contour, where the pseudogap suppresses strongly the spectral weight of the ARPES spectrum on the EFS contour at around the antinodal region, while it suppresses modestly the spectral weight at around the nodal region, leading to the formation of the disconnected Fermi arcs centered around the nodal region; (ii) the PDH structure in the

energy distribution curve, where the emergence of the dip in the PDH structure is due to the presence of the well-pronounced peak structure in the quasiparticle scattering rate (then the normal-state pseudogap); (iii) the notable checkerboard charge ordering in the underdoped pseudogap phase, where the checkerboard peaks found in the ARPES autocorrelation pattern are intimately related to the opening of the normal-state pseudogap. Our results therefore indicate that the *same spin excitation* that governs both the normal-state pseudogap-state and the SC-state naturally generates the exotic features of the low-energy electronic structure in the underdoped cuprate superconductors.

Acknowledgements

X.L. and S.P. are supported by the National Key Research and Development Program of China under Grant Nos. 2023YFA1406500 and 2021YFA1401803, and the National Natural Science Foundation of China (NSFC) under Grant No. 12274036. M.Z. is supported by NSFC under Grant No. 12247116 and the Special Funding for Postdoctoral Research Projects in Chongqing under Grant No. 2024CQBSHTB3156. H.G. acknowledge support from NSFC grant Nos. 11774019 and 12074022. This paper is written in honor of Professor Jan Zaanen, who has made many original works in the field of the high-temperature superconductivity research.

Appendix A: Derivation of Full electron diagonal and off-diagonal propagators

In this Appendix, our main goal is to derive the electron normal and anomalous self-energies in Eq. (5) of the main text [then the full electron diagonal and off-diagonal propagators $G(\mathbf{k}, \omega)$ and $\mathfrak{S}^\dagger(\mathbf{k}, \omega)$ in Eq. (3) of the main text] within the framework of the kinetic-energy-driven superconductivity by taking into account the vertex correction. The t - J model (1) in the fermion-spin representation (2) can be expressed as^{55,56},

$$H = \sum_{ll'} t_{ll'} (h_{l'\uparrow}^\dagger h_{l\uparrow} S_l^+ S_{l'}^- + h_{l'\downarrow}^\dagger h_{l\downarrow} S_l^- S_{l'}^+) - \mu_h \sum_{l\sigma} h_{l\sigma}^\dagger h_{l\sigma} + J_{\text{eff}} \sum_{\langle ll' \rangle} \mathbf{S}_l \cdot \mathbf{S}_{l'}, \quad (\text{A1})$$

with the charge-carrier chemical potential μ_h , $J_{\text{eff}} = (1 - \delta)^2 J$, and the charge-carrier doping concentration $\delta = \langle h_{l\sigma}^\dagger h_{l\sigma} \rangle$. As a natural consequence, the kinetic-energy term in the fermion-spin theory description of the t - J model (A1) has been converted into the strong coupling between charge and spin degrees of freedom of the constrained electron, which governs the essential physics of cuprate superconductors.

1. Mean-field formalism

In the mean-field (MF) approximation, the t - J model (A1) can be decoupled as^{55,56},

$$H_{\text{MF}} = H_t + H_J + H_0, \quad (\text{A2a})$$

$$H_t = \sum_{ll'} t_{ll'} \chi_{ll'} h_{l'\sigma}^\dagger h_{l\sigma} - \mu_h \sum_{l\sigma} h_{l\sigma}^\dagger h_{l\sigma}, \quad (\text{A2b})$$

$$H_J = \frac{1}{2} J_{\text{eff}} \sum_{\langle ll' \rangle} [S_l^+ S_{l'}^- + S_l^- S_{l'}^+ + 2S_l^z S_{l'}^z] + \sum_{ll'} t_{ll'} \phi_{ll'} (S_l^+ S_{l'}^- + S_l^- S_{l'}^+), \quad (\text{A2c})$$

where $H_0 = -2 \sum_{ll'} t_{ll'} \chi_{ll'} \phi_{ll'}$, the charge-carrier's particle-hole parameter $\phi_{ll'} = \langle h_{l'\sigma}^\dagger h_{l\sigma} \rangle$, and the spin correlation function $\chi_{ll'} = \langle S_l^+ S_{l'}^- \rangle$.

With the help of the above charge-carrier part (A2b), the MF charge-carrier propagator is obtained straightforwardly as^{55,56},

$$g^{(0)}(\mathbf{k}, \omega) = \frac{1}{\omega - \xi_{\mathbf{k}}}, \quad (\text{A3})$$

where the MF charge-carrier energy dispersion is given explicitly as,

$$\xi_{\mathbf{k}} = 4\chi_1 t \gamma_{\mathbf{k}} - 4\chi_2 t' \gamma'_{\mathbf{k}} - \mu_h, \quad (\text{A4})$$

with $\chi_1 = \langle S_l^+ S_{l+\hat{\eta}}^- \rangle$ and $\chi_2 = \langle S_l^+ S_{l+\hat{\tau}}^- \rangle$.

Now we turn to derive the spin propagator in the MF approximation. In the doped regime without an anti-ferromagnetic long-range order (AFLRO), i.e., $\langle S_l^z \rangle = 0$, the spin propagator can be calculated in terms of the Kondo-Yamaji decoupling approximation¹⁰⁴, which is a stage one-step further than the Tyablikov's decoupling approximation¹⁰⁵. However, in the MF level, the spin part (A2c) is an anisotropic Heisenberg model, we therefore need two spin propagators $D(l - l', t - t') = -i\theta(t - t') \langle [S_l^+(t), S_{l'}^-(t')] \rangle = \langle \langle S_l^+(t); S_{l'}^-(t') \rangle \rangle$ and $D_z(l - l', t - t') = -i\theta(t - t') \langle [S_l^z(t), S_{l'}^z(t')] \rangle = \langle \langle S_l^z(t); S_{l'}^z(t') \rangle \rangle$ to give a proper description of the essential properties of the spin excitation^{55,56}. According to the previous discussions^{55,56}, the spin propagators $D^{(0)}(\mathbf{k}, \omega)$ and $D_z^{(0)}(\mathbf{k}, \omega)$ in the MF approximation can be calculated straightforwardly as,

$$D^{(0)}(\mathbf{k}, \omega) = \frac{B_{\mathbf{k}}}{2\omega_{\mathbf{k}}} \left(\frac{1}{\omega - \omega_{\mathbf{k}}} - \frac{1}{\omega + \omega_{\mathbf{k}}} \right), \quad (\text{A5a})$$

$$D_z^{(0)}(\mathbf{k}, \omega) = \frac{B_{\mathbf{k}}^{(z)}}{2\omega_{\mathbf{k}}^{(z)}} \left(\frac{1}{\omega - \omega_{\mathbf{k}}^{(z)}} - \frac{1}{\omega + \omega_{\mathbf{k}}^{(z)}} \right), \quad (\text{A5b})$$

respectively, where the spin excitation spectra $\omega_{\mathbf{k}}$ and $\omega_{\mathbf{k}}^{(z)}$ in the MF approximation are respectively expressed as,

$$\begin{aligned} \omega_{\mathbf{k}}^2 &= \alpha\lambda_1^2 \left[\frac{1}{2}\epsilon\chi_1(A_{11} - \gamma_{\mathbf{k}})(\epsilon - \gamma_{\mathbf{k}}) + \chi_1^z(A_{12} - \epsilon\gamma_{\mathbf{k}})(1 - \epsilon\gamma_{\mathbf{k}}) \right] + \alpha\lambda_2^2 \left[\left(\chi_2^z\gamma'_{\mathbf{k}} - \frac{3}{8}\chi_2 \right) \gamma'_{\mathbf{k}} + A_{13} \right] \\ &+ \alpha\lambda_1\lambda_2 \left[(\chi_1^z + \chi_2^z)(A_{14} - \epsilon\gamma_{\mathbf{k}})\gamma'_{\mathbf{k}} + \frac{1}{2}(\chi_1\gamma'_{\mathbf{k}} - C_3)(\epsilon - \gamma_{\mathbf{k}}) - \frac{1}{2}\epsilon(C_3 - \chi_2\gamma_{\mathbf{k}}) \right], \end{aligned} \quad (\text{A6a})$$

$$(\omega_{\mathbf{k}}^{(z)})^2 = \alpha\epsilon\lambda_1^2(A_{15} - \gamma_{\mathbf{k}})(1 - \gamma_{\mathbf{k}}) + \alpha\lambda_2^2 A_{16}(1 - \gamma'_{\mathbf{k}}) + \alpha\lambda_1\lambda_2[\epsilon C_3(\gamma_{\mathbf{k}} - 1) + (\chi_2\gamma_{\mathbf{k}} - \epsilon C_3)(1 - \gamma'_{\mathbf{k}})], \quad (\text{A6b})$$

while the corresponding weight functions $B_{\mathbf{k}}$ and $B_{z\mathbf{k}}$ are respectively given as,

$$\begin{aligned} B_{\mathbf{k}} &= \lambda_1[2\chi_1^z(\epsilon\gamma_{\mathbf{k}} - 1) + \chi_1(\gamma_{\mathbf{k}} - \epsilon)] \\ &- \lambda_2(2\chi_2^z\gamma'_{\mathbf{k}} - \chi_2), \end{aligned} \quad (\text{A7a})$$

$$B_{\mathbf{k}}^{(z)} = \epsilon\chi_1\lambda_1(\gamma_{\mathbf{k}} - 1) - \chi_2\lambda_2(\gamma'_{\mathbf{k}} - 1), \quad (\text{A7b})$$

with $\lambda_1 = 8J_{\text{eff}}$, $\lambda_2 = 16\phi_2 t'$, $\epsilon = 1 + 2t\phi_1/J_{\text{eff}}$, $\phi_1 = \langle h_{l\sigma}^\dagger h_{l+\hat{\eta}\sigma} \rangle$, $\phi_2 = \langle h_{l\sigma}^\dagger h_{l+\hat{\tau}\sigma} \rangle$, $A_{11} = [(1-\alpha)/(8\alpha) - \chi_1^z/2 + C_1]/\chi_1$, $A_{12} = [(1-\alpha)/(16\alpha) - \epsilon\chi_1/8 + C_1^z]/\chi_1^z$, $A_{13} = [(1-\alpha)/(8\alpha) - \chi_2^z/2 + C_2]/2$, $A_{14} = (\chi_1^z + C_3)/[\epsilon(\chi_1^z + \chi_2^z)]$, $A_{15} = \epsilon[(1-\alpha)/(8\alpha) + C_1]/\chi_1$, $A_{16} = (1-\alpha)/(8\alpha) + C_3$, the spin correlation functions $\chi_1^z = \langle S_l^z S_{l+\hat{\eta}}^z \rangle$, $\chi_2^z = \langle S_l^z S_{l+\hat{\tau}}^z \rangle$, $C_1 = (1/16) \sum_{\hat{\eta}, \hat{\eta}'} \langle S_{l+\hat{\eta}}^+ S_{l+\hat{\eta}'}^- \rangle$, $C_1^z = (1/16) \sum_{\hat{\eta}, \hat{\eta}'} \langle S_{l+\hat{\eta}}^z S_{l+\hat{\eta}'}^z \rangle$, $C_2 = (1/16) \sum_{\hat{\tau}, \hat{\tau}'} \langle S_{l+\hat{\tau}}^+ S_{l+\hat{\tau}'}^- \rangle$, $C_3 = (1/4) \sum_{\hat{\tau}} \langle S_{l+\hat{\tau}}^+ S_{l+\hat{\tau}}^- \rangle$, and $C_3^z = (1/4) \sum_{\hat{\tau}} \langle S_{l+\hat{\tau}}^z S_{l+\hat{\tau}}^z \rangle$. In order to fulfill the sum rule of the spin correlation function $\langle S_l^+ S_l^- \rangle = 1/2$ in the case without an AFLRO, the crucial decoupling parameter α has been introduced in the above calculation^{55,56,104}, which can be regarded as the vertex correction. At the half-filling, the t - J model (A1) is reduced as an isotropic Heisenberg model, and the degree of freedom is local spin only, where $\epsilon = 1$, $\lambda_2 = 0$, $\chi_1^z = \chi_1/2$, $C_1^z = C_1/2$, and then the above spin excitation energy dispersion $\omega_{\mathbf{k}}$ and the weight function $B_{\mathbf{k}}$ are respectively reduced as, $\omega_{\mathbf{k}} = \lambda_1 \sqrt{\alpha} |\chi_1| (1 - \gamma_{\mathbf{k}}^2)$ and $B_{\mathbf{k}} = -2\lambda_1\chi_1(1 - \gamma_{\mathbf{k}})$. This spin excitation energy dispersion at the half-filling is the standard spin-wave dispersion. However, in the doped regime without an AFLRO, although the form of the spin excitation energy dispersion $\omega_{\mathbf{k}}$ in Eq. (A6a) is rather complicated, the essential properties of the spin-wave nature are the same as that in the case of the half-filling^{55,56}.

2. Charge-carrier normal and anomalous self-energies

In the framework of the kinetic-energy-driven superconductivity^{56,71,72}, the spin-excitation mediates the charge-carrier interaction directly from the kinetic energy of the t - J model (A1), and then this charge-carrier interaction induces the charge-carrier pairing state in the particle-particle channel and charge-carrier pseudogap-state in the particle-hole channel, where the

self-consistent equations that are satisfied by the full charge-carrier diagonal and off-diagonal propagators of the t - J model (A1) are respectively derived as,

$$\begin{aligned} g(\mathbf{k}, \omega) &= g^{(0)}(\mathbf{k}, \omega) + g^{(0)}(\mathbf{k}, \omega) [\Sigma_{\text{ph}}^{(h)}(\mathbf{k}, \omega) g(\mathbf{k}, \omega) \\ &- \Sigma_{\text{pp}}^{(h)}(\mathbf{k}, \omega) \Gamma^\dagger(\mathbf{k}, \omega)], \end{aligned} \quad (\text{A8a})$$

$$\begin{aligned} \Gamma^\dagger(\mathbf{k}, \omega) &= g^{(0)}(\mathbf{k}, -\omega) [\Sigma_{\text{ph}}^{(h)}(\mathbf{k}, -\omega) \Gamma^\dagger(\mathbf{k}, \omega) \\ &+ \Sigma_{\text{pp}}^{(h)}(\mathbf{k}, \omega) g(\mathbf{k}, \omega)], \end{aligned} \quad (\text{A8b})$$

and then the full charge-carrier diagonal and off-diagonal propagators $g(\mathbf{k}, \omega)$ and $\Gamma^\dagger(\mathbf{k}, \omega)$ are respectively expressed explicitly as,

$$g(\mathbf{k}, \omega) = \frac{1}{\omega - \xi_{\mathbf{k}} - \Sigma_{\text{tot}}^{(h)}(\mathbf{k}, \omega)}, \quad (\text{A9a})$$

$$\Gamma^\dagger(\mathbf{k}, \omega) = \frac{W_{\text{h}}(\mathbf{k}, \omega)}{\omega - \xi_{\mathbf{k}} - \Sigma_{\text{tot}}^{(h)}(\mathbf{k}, \omega)}, \quad (\text{A9b})$$

where the charge-carrier total self-energy $\Sigma_{\text{tot}}^{(h)}(\mathbf{k}, \omega)$ and the function $W_{\text{h}}(\mathbf{k}, \omega)$ are given as,

$$\Sigma_{\text{tot}}^{(h)}(\mathbf{k}, \omega) = \Sigma_{\text{ph}}^{(h)}(\mathbf{k}, \omega) + \frac{|\Sigma_{\text{pp}}^{(h)}(\mathbf{k}, \omega)|^2}{\omega + \xi_{\mathbf{k}} + \Sigma_{\text{ph}}^{(h)}(\mathbf{k}, -\omega)}, \quad (\text{A10a})$$

$$W_{\text{h}}(\mathbf{k}, \omega) = -\frac{\Sigma_{\text{pp}}^{(h)}(\mathbf{k}, \omega)}{\omega + \xi_{\mathbf{k}} + \Sigma_{\text{ph}}^{(h)}(\mathbf{k}, -\omega)}, \quad (\text{A10b})$$

respectively, with the charge-carrier normal self-energy $\Sigma_{\text{ph}}^{(h)}(\mathbf{k}, \omega)$ in the particle-hole channel and the charge-carrier anomalous self-energy $\Sigma_{\text{pp}}^{(h)}(\mathbf{k}, \omega)$ in the particle-particle channel, which have been evaluated in terms of the spin bubble as^{56,71,72},

$$\begin{aligned} \Sigma_{\text{ph}}^{(h)}(\mathbf{k}, i\omega_n) &= \frac{1}{N^2} \sum_{\mathbf{p}, \mathbf{p}'} \Lambda_{\mathbf{p}+\mathbf{p}'+\mathbf{k}}^2 \\ &\times \frac{1}{\beta} \sum_{ip_m} g(\mathbf{p} + \mathbf{k}, ip_m + i\omega_n) \Pi(\mathbf{p}, \mathbf{p}', ip_m), \end{aligned} \quad (\text{A11a})$$

$$\begin{aligned} \Sigma_{\text{pp}}^{(h)}(\mathbf{k}, i\omega_n) &= \frac{1}{N^2} \sum_{\mathbf{p}, \mathbf{p}'} \Lambda_{\mathbf{p}+\mathbf{p}'+\mathbf{k}}^2 \\ &\times \frac{1}{\beta} \sum_{ip_m} \Gamma^\dagger(\mathbf{p} + \mathbf{k}, ip_m + i\omega_n) \Pi(\mathbf{p}, \mathbf{p}', ip_m), \end{aligned} \quad (\text{A11b})$$

respectively, where ω_n and p_m are the fermion and boson Matsubara frequencies, respectively. The above charge-carrier self-energies in Eq. (A11) are induced by the coupling between charge and spin degrees of freedom of the constrained electron directly from the kinetic energy of the t - J model (A1) in the fermion-spin representation⁵⁶, where the bare vertex function $\Lambda_{\mathbf{k}} = 4t\gamma_{\mathbf{k}} - 4t'\gamma'_{\mathbf{k}}$ is originated from the derivation of these charge-carrier self-energies in the random phase approximation. The spin bubble $\Pi(\mathbf{p}, \mathbf{p}', ip_m)$ is obtained in terms of the spin propagator $D^{(0)}(\mathbf{k}, \omega)$ in Eq. (A5a) as,

$$\Pi(\mathbf{p}, \mathbf{p}', ip_m) = \frac{1}{\beta} \sum_{ip'_m} D^{(0)}(\mathbf{p}', ip'_m) D^{(0)}(\mathbf{p}' + \mathbf{p}, ip'_m + ip_m). \quad (\text{A12})$$

The charge-carrier anomalous self-energy $\Sigma_{\text{pp}}^{(\text{h})}(\mathbf{k}, \omega)$ is identified as the momentum and energy dependence of the charge-carrier pair gap, i.e., $\Sigma_{\text{pp}}^{(\text{h})}(\mathbf{k}, \omega) = \bar{\Delta}_{\mathbf{k}}^{(\text{h})}(\omega)$, while the charge-carrier normal self-energy $\Sigma_{\text{ph}}^{(\text{h})}(\mathbf{k}, \omega)$ describes the momentum and energy dependence of the charge-carrier single-particle coherence. Although $\Sigma_{\text{pp}}^{(\text{h})}(\mathbf{k}, \omega)$ is an even function of energy, $\Sigma_{\text{ph}}^{(\text{h})}(\mathbf{k}, \omega)$ is not. In this case, $\Sigma_{\text{ph}}^{(\text{h})}(\mathbf{k}, \omega)$ can be divided into its symmetric and antisymmetric parts as: $\Sigma_{\text{ph}}^{(\text{h})}(\mathbf{k}, \omega) = \Sigma_{\text{phe}}^{(\text{h})}(\mathbf{k}, \omega) + \omega \Sigma_{\text{pho}}^{(\text{h})}(\mathbf{k}, \omega)$, and then both $\Sigma_{\text{phe}}^{(\text{h})}(\mathbf{k}, \omega)$ and $\Sigma_{\text{pho}}^{(\text{h})}(\mathbf{k}, \omega)$ are an even function of energy. Furthermore, this antisymmetric part $\Sigma_{\text{pho}}^{(\text{h})}(\mathbf{k}, \omega)$ is correlated directly with the momentum and energy dependence of the charge-carrier single-particle coherent weight as: $Z_{\text{F}}^{(\text{h})-1}(\mathbf{k}, \omega) = 1 - \text{Re}\Sigma_{\text{pho}}^{(\text{h})}(\mathbf{k}, \omega)$. In this paper, we focus mainly on the anomalous properties of the low-energy electronic structure, and then $\bar{\Delta}_{\mathbf{k}}^{(\text{h})}(\omega)$ and $Z_{\text{F}}^{(\text{h})}(\mathbf{k}, \omega)$ can be discussed in the static limit, i.e.,

$$\bar{\Delta}_{\mathbf{k}}^{(\text{h})} = \bar{\Delta}_{\text{h}}\gamma_{\mathbf{k}}^{(\text{d})}, \quad (\text{A13a})$$

$$\frac{1}{Z_{\text{F}}^{(\text{h})}(\mathbf{k})} = 1 - \text{Re}\Sigma_{\text{pho}}^{(\text{h})}(\mathbf{k}, \omega) |_{\omega=0}, \quad (\text{A13b})$$

with the charge-carrier pair gap parameter $\bar{\Delta}_{\text{h}}$. Although $Z_{\text{F}}^{(\text{h})}(\mathbf{k})$ still is a function of momentum, the momentum dependence is unimportant in a qualitative discussion. Following the ARPES experiments^{106,107}, the momentum \mathbf{k} in $Z_{\text{F}}^{(\text{h})}(\mathbf{k})$ can be chosen as,

$$Z_{\text{F}}^{(\text{h})} = Z_{\text{F}}^{(\text{h})}(\mathbf{k}) |_{\mathbf{k}=[\pi,0]}. \quad (\text{A14})$$

With the above static-limit approximation, the renormalized charge-carrier diagonal and off-diagonal propagators now can be obtained from Eq. (A9) as,

$$g^{(\text{RMF})}(\mathbf{k}, \omega) = Z_{\text{F}}^{(\text{h})} \left(\frac{U_{\text{h}}^2(\mathbf{k})}{\omega - E_{\mathbf{k}}^{(\text{h})}} + \frac{V_{\text{h}}^2(\mathbf{k})}{\omega + E_{\mathbf{k}}^{(\text{h})}} \right), \quad (\text{A15a})$$

$$\Gamma^{(\text{RMF})\dagger}(\mathbf{k}, \omega) = -Z_{\text{F}}^{(\text{h})} \frac{\bar{\Delta}_{\text{Zk}}^{(\text{h})}}{2E_{\mathbf{k}}^{(\text{h})}} \left(\frac{1}{\omega - E_{\mathbf{k}}^{(\text{h})}} - \frac{1}{\omega + E_{\mathbf{k}}^{(\text{h})}} \right), \quad (\text{A15b})$$

with the charge-carrier quasiparticle energy dispersion $E_{\mathbf{k}}^{(\text{h})} = \sqrt{\bar{\xi}_{\mathbf{k}}^2 + |\bar{\Delta}_{\text{Zk}}^{(\text{h})}|^2}$, the renormalized MF charge-carrier energy dispersion $\bar{\xi}_{\mathbf{k}} = Z_{\text{F}}^{(\text{h})}\xi_{\mathbf{k}}$, the renormalized charge-carrier pair gap $\bar{\Delta}_{\text{Zk}}^{(\text{h})} = Z_{\text{F}}^{(\text{h})}\bar{\Delta}_{\mathbf{k}}^{(\text{h})}$, and the charge-carrier quasiparticle coherence factors,

$$U_{\text{h}}^2(\mathbf{k}) = \frac{1}{2} \left(1 + \frac{\bar{\xi}_{\mathbf{k}}}{E_{\mathbf{k}}^{(\text{h})}} \right), \quad (\text{A16a})$$

$$V_{\text{h}}^2(\mathbf{k}) = \frac{1}{2} \left(1 - \frac{\bar{\xi}_{\mathbf{k}}}{E_{\mathbf{k}}^{(\text{h})}} \right), \quad (\text{A16b})$$

which satisfy the constraint $U_{\text{h}}^2(\mathbf{k}) + V_{\text{h}}^2(\mathbf{k}) = 1$ for any momentum \mathbf{k} .

Substituting the renormalized charge-carrier diagonal and off-diagonal propagators in Eq. (A15) and spin propagator in Eq. (A5a) into Eq. (A11), the charge-carrier normal self-energy $\Sigma_{\text{ph}}^{(\text{h})}(\mathbf{k}, \omega)$ and the anomalous self-energy $\Sigma_{\text{pp}}^{(\text{h})}(\mathbf{k}, \omega)$ can be respectively derived as,

$$\begin{aligned} \Sigma_{\text{ph}}^{(\text{h})}(\mathbf{k}, \omega) &= \frac{Z_{\text{F}}^{(\text{h})}}{N^2} \sum_{\mathbf{pp}'\nu} (-1)^{\nu+1} \Omega_{\mathbf{pp}'\mathbf{k}} \left[U_{\text{h}}^2(\mathbf{p} + \mathbf{k}) \left(\frac{F_{1\nu}^{(\text{h})}(\mathbf{p}, \mathbf{p}', \mathbf{k})}{\omega + \omega_{\mathbf{pp}'}^{(\nu)} - E_{\mathbf{p}+\mathbf{k}}^{(\text{h})}} - \frac{F_{2\nu}^{(\text{h})}(\mathbf{p}, \mathbf{p}', \mathbf{k})}{\omega - \omega_{\mathbf{pp}'}^{(\nu)} - E_{\mathbf{p}+\mathbf{k}}^{(\text{h})}} \right) \right. \\ &\quad \left. + V_{\text{h}}^2(\mathbf{p} + \mathbf{k}) \left(\frac{F_{1\nu}^{(\text{h})}(\mathbf{p}, \mathbf{p}', \mathbf{k})}{\omega - \omega_{\mathbf{pp}'}^{(\nu)} + E_{\mathbf{p}+\mathbf{k}}^{(\text{h})}} - \frac{F_{2\nu}^{(\text{h})}(\mathbf{p}, \mathbf{p}', \mathbf{k})}{\omega + \omega_{\mathbf{pp}'}^{(\nu)} + E_{\mathbf{p}+\mathbf{k}}^{(\text{h})}} \right) \right], \end{aligned} \quad (\text{A17a})$$

$$\begin{aligned} \Sigma_{\text{pp}}^{(\text{h})}(\mathbf{k}, \omega) &= \frac{Z_{\text{F}}^{(\text{h})}}{N^2} \sum_{\mathbf{pp}'\nu} (-1)^{\nu} \Omega_{\mathbf{pp}'\mathbf{k}} \frac{\bar{\Delta}_{\text{Zp+k}}^{(\text{h})}}{2E_{\mathbf{p+k}}^{(\text{h})}} \left[\left(\frac{F_{1\nu}^{(\text{h})}(\mathbf{p}, \mathbf{p}', \mathbf{k})}{\omega + \omega_{\mathbf{pp}'}^{(\nu)} - E_{\mathbf{p+k}}^{(\text{h})}} - \frac{F_{2\nu}^{(\text{h})}(\mathbf{p}, \mathbf{p}', \mathbf{k})}{\omega - \omega_{\mathbf{pp}'}^{(\nu)} - E_{\mathbf{p+k}}^{(\text{h})}} \right) \right. \\ &\quad \left. - \left(\frac{F_{1\nu}^{(\text{h})}(\mathbf{p}, \mathbf{p}', \mathbf{k})}{\omega - \omega_{\mathbf{pp}'}^{(\nu)} + E_{\mathbf{p+k}}^{(\text{h})}} - \frac{F_{2\nu}^{(\text{h})}(\mathbf{p}, \mathbf{p}', \mathbf{k})}{\omega + \omega_{\mathbf{pp}'}^{(\nu)} + E_{\mathbf{p+k}}^{(\text{h})}} \right) \right], \end{aligned} \quad (\text{A17b})$$

with $\nu = 1, 2$, the kernel function $\Omega_{\mathbf{pp}'\mathbf{k}} = [\Lambda_{\mathbf{p}+\mathbf{p}'+\mathbf{k}}]^2 B_{\mathbf{p}'} B_{\mathbf{p}+\mathbf{p}'}/(4\omega_{\mathbf{p}'}\omega_{\mathbf{p}+\mathbf{p}'})$, $\omega_{\mathbf{pp}'}^{(\nu)} = \omega_{\mathbf{p}+\mathbf{p}'} - (-1)^{\nu}\omega_{\mathbf{p}'}$, and the

functions,

$$F_{1\nu}^{(h)}(\mathbf{p}, \mathbf{p}', \mathbf{k}) = n_F[E_{\mathbf{p}+\mathbf{k}}^{(h)}]\{1 + n_B(\omega_{\mathbf{p}'+\mathbf{p}}) + n_B[(-1)^{\nu+1}\omega_{\mathbf{p}'}]\} + n_B(\omega_{\mathbf{p}'+\mathbf{p}})n_B[(-1)^{\nu+1}\omega_{\mathbf{p}'}], \quad (\text{A18a})$$

$$F_{2\nu}^{(h)}(\mathbf{p}, \mathbf{p}', \mathbf{k}) = \{1 - n_F[E_{\mathbf{p}+\mathbf{k}}^{(h)}]\}\{1 + n_B(\omega_{\mathbf{p}'+\mathbf{p}}) + n_B[(-1)^{\nu+1}\omega_{\mathbf{p}'}]\} + n_B(\omega_{\mathbf{p}'+\mathbf{p}})n_B[(-1)^{\nu+1}\omega_{\mathbf{p}'}], \quad (\text{A18b})$$

where $n_B(\omega)$ and $n_F(\omega)$ are the boson and fermion distribution functions, respectively.

3. Self-consistent equations for determination of charge-carrier order parameters

The above charge-carrier single-particle coherent weight $Z_F^{(h)}$ and the charge-carrier pair gap parameter $\bar{\Delta}_h$ respectively satisfy following two self-consistent equations,

$$\frac{1}{Z_F^{(h)}} = 1 + \frac{Z_F^{(h)}}{N^2} \sum_{\mathbf{p}\mathbf{p}'\nu} (-1)^{\nu+1} \Omega_{\mathbf{p}\mathbf{p}'\mathbf{k}_A} \left(\frac{F_{1\nu}^{(h)}(\mathbf{p}, \mathbf{p}', \mathbf{k}_A)}{[\omega_{\mathbf{p}\mathbf{p}'}^{(\nu)} - E_{\mathbf{p}+\mathbf{k}_A}^{(h)}]^2} + \frac{F_{2\nu}^{(h)}(\mathbf{p}, \mathbf{p}', \mathbf{k}_A)}{[\omega_{\mathbf{p}\mathbf{p}'}^{(\nu)} + E_{\mathbf{p}+\mathbf{k}_A}^{(h)}]^2} \right), \quad (\text{A19a})$$

$$1 = \frac{4[Z_F^{(h)}]^2}{N^3} \sum_{\mathbf{p}\mathbf{p}'\mathbf{k}\nu} (-1)^\nu \Omega_{\mathbf{p}\mathbf{p}'\mathbf{k}} \frac{\gamma_{\mathbf{k}}^{(d)} \gamma_{\mathbf{p}+\mathbf{k}}^{(d)}}{E_{\mathbf{p}+\mathbf{k}}^{(h)}} \left(\frac{F_{1\nu}^{(h)}(\mathbf{p}, \mathbf{p}', \mathbf{k})}{\omega_{\mathbf{p}\mathbf{p}'}^{(\nu)} - E_{\mathbf{p}+\mathbf{k}}^{(h)}} - \frac{F_{2\nu}^{(h)}(\mathbf{p}, \mathbf{p}', \mathbf{k})}{\omega_{\mathbf{p}\mathbf{p}'}^{(\nu)} + E_{\mathbf{p}+\mathbf{k}}^{(h)}} \right), \quad (\text{A19b})$$

where $\mathbf{k}_A = [\pi, 0]$. The above two self-consistent equations must be solved simultaneously with following self-consistent equations,

$$\phi_1 = \frac{Z_F^{(h)}}{2N} \sum_{\mathbf{k}} \gamma_{\mathbf{k}} \left(1 - \frac{\bar{\xi}_{\mathbf{k}}}{E_{\mathbf{k}}^{(h)}} \tanh\left[\frac{1}{2}\beta E_{\mathbf{k}}^{(h)}\right] \right), \quad (\text{A20a})$$

$$\phi_2 = \frac{Z_F^{(h)}}{2N} \sum_{\mathbf{k}} \gamma'_{\mathbf{k}} \left(1 - \frac{\bar{\xi}_{\mathbf{k}}}{E_{\mathbf{k}}^{(h)}} \tanh\left[\frac{1}{2}\beta E_{\mathbf{k}}^{(h)}\right] \right), \quad (\text{A20b})$$

$$\delta = \frac{Z_F^{(h)}}{2N} \sum_{\mathbf{k}} \left(1 - \frac{\bar{\xi}_{\mathbf{k}}}{E_{\mathbf{k}}^{(h)}} \tanh\left[\frac{1}{2}\beta E_{\mathbf{k}}^{(h)}\right] \right), \quad (\text{A20c})$$

$$\chi_1 = \frac{1}{N} \sum_{\mathbf{k}} \gamma_{\mathbf{k}} \frac{B_{\mathbf{k}}}{2\omega_{\mathbf{k}}} \coth\left[\frac{1}{2}\beta\omega_{\mathbf{k}}\right], \quad (\text{A20d})$$

$$\chi_2 = \frac{1}{N} \sum_{\mathbf{k}} \gamma'_{\mathbf{k}} \frac{B_{\mathbf{k}}}{2\omega_{\mathbf{k}}} \coth\left[\frac{1}{2}\beta\omega_{\mathbf{k}}\right], \quad (\text{A20e})$$

$$C_1 = \frac{1}{N} \sum_{\mathbf{k}} \gamma_{\mathbf{k}}^2 \frac{B_{\mathbf{k}}}{2\omega_{\mathbf{k}}} \coth\left[\frac{1}{2}\beta\omega_{\mathbf{k}}\right], \quad (\text{A20f})$$

$$C_2 = \frac{1}{N} \sum_{\mathbf{k}} \gamma_{\mathbf{k}}'^2 \frac{B_{\mathbf{k}}}{2\omega_{\mathbf{k}}} \coth\left[\frac{1}{2}\beta\omega_{\mathbf{k}}\right], \quad (\text{A20g})$$

$$C_3 = \frac{1}{N} \sum_{\mathbf{k}} \gamma_{\mathbf{k}} \gamma'_{\mathbf{k}} \frac{B_{\mathbf{k}}}{2\omega_{\mathbf{k}}} \coth\left[\frac{1}{2}\beta\omega_{\mathbf{k}}\right], \quad (\text{A20h})$$

$$\frac{1}{2} = \frac{1}{N} \sum_{\mathbf{k}} \frac{B_{\mathbf{k}}}{2\omega_{\mathbf{k}}} \coth\left[\frac{1}{2}\beta\omega_{\mathbf{k}}\right], \quad (\text{A20i})$$

$$\chi_1^z = \frac{1}{N} \sum_{\mathbf{k}} \gamma_{\mathbf{k}} \frac{B_{\mathbf{k}}^{(z)}}{2\omega_{\mathbf{k}}^{(z)}} \coth\left[\frac{1}{2}\beta\omega_{\mathbf{k}}^{(z)}\right], \quad (\text{A20j})$$

$$\chi_2^z = \frac{1}{N} \sum_{\mathbf{k}} \gamma'_{\mathbf{k}} \frac{B_{\mathbf{k}}^{(z)}}{2\omega_{\mathbf{k}}^{(z)}} \coth\left[\frac{1}{2}\beta\omega_{\mathbf{k}}^{(z)}\right], \quad (\text{A20k})$$

$$C_1^z = \frac{1}{N} \sum_{\mathbf{k}} \gamma_{\mathbf{k}}^2 \frac{B_{\mathbf{k}}^{(z)}}{2\omega_{\mathbf{k}}^{(z)}} \coth\left[\frac{1}{2}\beta\omega_{\mathbf{k}}^{(z)}\right], \quad (\text{A20l})$$

$$C_3^z = \frac{1}{N} \sum_{\mathbf{k}} \gamma_{\mathbf{k}} \gamma'_{\mathbf{k}} \frac{B_{\mathbf{k}}^{(z)}}{2\omega_{\mathbf{k}}^{(z)}} \coth\left[\frac{1}{2}\beta\omega_{\mathbf{k}}^{(z)}\right], \quad (\text{A20m})$$

and then all the above order parameters, charge-carrier's particle-hole parameters, spin correlation functions, decoupling parameter α , and charge-carrier chemical potential μ_h are determined by the self-consistent calculation *without using any adjustable parameters*.

The above self-consistent equations (A19) and (A20) have been calculated at different doping concentrations^{56,71,72}, and the result shows that the charge-carrier pair gap parameter $\bar{\Delta}_h$ exhibits a dome-like shape doping dependence, i.e., with the increase of doping, $\bar{\Delta}_h$ is raised gradually in the underdoped regime, and reaches its maximum at around the optimal doping $\delta \approx 0.15$, then with a further increase of doping, $\bar{\Delta}_h$ turns into a monotonically decreases in the overdoped regime. It should be emphasized that the above parameters determined by the self-consistent equation (A20), including the charge-carrier's particle-hole parameters $\phi_1 = \langle h_{l\sigma}^\dagger h_{l+\hat{\eta}\sigma} \rangle$ and $\phi_2 = \langle h_{l\sigma}^\dagger h_{l+\hat{\tau}\sigma} \rangle$, the spin correlation functions $\chi_1 = \langle S_l^+ S_{l+\hat{\eta}}^- \rangle$, $\chi_2 = \langle S_l^+ S_{l+\hat{\tau}}^- \rangle$, $\chi_1^z = \langle S_l^z S_{l+\hat{\eta}}^z \rangle$, $\chi_2^z = \langle S_l^z S_{l+\hat{\tau}}^z \rangle$, $C_1 = (1/Z^2) \sum_{\hat{\eta}, \hat{\eta}'} \langle S_{l+\hat{\eta}}^+ S_{l+\hat{\eta}'}^- \rangle$, $C_1^z = (1/Z^2) \sum_{\hat{\eta}, \hat{\eta}'} \langle S_{l+\hat{\eta}}^z S_{l+\hat{\eta}'}^z \rangle$, $C_2 = (1/Z^2) \sum_{\hat{\tau}, \hat{\tau}'} \langle S_{l+\hat{\tau}}^+ S_{l+\hat{\tau}'}^- \rangle$, $C_3 = (1/Z) \sum_{\hat{\tau}} \langle S_{l+\hat{\eta}}^+ S_{l+\hat{\tau}}^- \rangle$, $C_3^z = (1/Z) \sum_{\hat{\tau}} \langle S_{l+\hat{\eta}}^z S_{l+\hat{\tau}}^z \rangle$, and the decoupling parameter α in the Kondo-Yamaji decoupling approximation¹⁰⁴ for the derivation of the spin propagators in Eq. (A5), are essential MF parameters for the description of the charge-carrier and spin parts of the MF t - J model in Eq. (A2), and therefore the magni-

tude of these parameters are finite both in the pseudogap phase (then the normal-state) and SC-state.

4. Charge-carrier pair transition temperature

The charge-carrier pair gap $\bar{\Delta}_h$ is strongly temperature dependent, and vanishes at the charge-carrier pair transition temperature $T_c^{(\text{pair})}$. This $T_c^{(\text{pair})}$ has been also evaluated self-consistently at different doping concentrations^{56,71,72}, and the calculated result shows that $T_c^{(\text{pair})}$ as a function of doping presents a similar behavior of $\bar{\Delta}_h$, i.e., the maximal $T_c^{(\text{pair})}$ emerges at around the optimal doping $\delta \approx 0.15$, and then decreases in both the underdoped and the overdoped regimes. Moreover, we⁷³ have shown that the magnitude of $T_c^{(\text{pair})}$ is exactly the same as the corresponding one of the SC transition temperature T_c derived from the electron pairing state at the condition of the electron pair gap parameter $\bar{\Delta} = 0$, and we will return to this discussion of $T_c^{(\text{pair})}$ towards subsection A 8 of this Appendix.

5. Pseudogap in charge channel

To explore the nature of the pseudogap in the charge channel, we rewrite the charge-carrier normal self-energy in Eq. (A17a) as,

$$\Sigma_{\text{ph}}^{(\text{h})}(\mathbf{k}, \omega) \approx \frac{[2\bar{\Delta}_{\text{pg}}^{(\text{h})}(\mathbf{k})]^2}{\omega - \xi_{0\mathbf{k}}}, \quad (\text{A21})$$

where $\xi_{0\mathbf{k}} = L_2^{(\text{h})}(\mathbf{k})/L_1^{(\text{h})}(\mathbf{k})$ is the energy spectrum of $\Sigma_{\text{ph}}^{(\text{h})}(\mathbf{k}, \omega)$, while $\bar{\Delta}_{\text{pg}}^{(\text{h})}(\mathbf{k}) = L_2^{(\text{h})}(\mathbf{k})/\sqrt{4L_1^{(\text{h})}(\mathbf{k})}$ is referred to as the momentum dependence of the charge-carrier pseudogap, since it plays a role of the suppression of the charge-carrier density of states. The functions $L_1^{(\text{h})}(\mathbf{k}) = -\Sigma_{\text{pho}}^{(\text{h})}(\mathbf{k}, \omega = 0)$ and $L_2^{(\text{h})}(\mathbf{k}) = -\Sigma_{\text{ph}}^{(\text{h})}(\mathbf{k}, \omega = 0)$, while $\Sigma_{\text{ph}}^{(\text{h})}(\mathbf{k}, \omega = 0)$ and the antisymmetric part $\Sigma_{\text{pho}}^{(\text{h})}(\mathbf{k}, \omega)$ of the charge-carrier normal self-energy are calculated directly from $\Sigma_{\text{ph}}^{(\text{h})}(\mathbf{k}, \omega)$ in Eq. (A17a). In this case, it is straightforward to obtain the charge-carrier pseudogap parameter as $\bar{\Delta}_{\text{pg}}^{(\text{h})} = (1/N) \sum_{\mathbf{k}} \bar{\Delta}_{\text{pg}}^{(\text{h})}(\mathbf{k})$.

In the previous discussions^{56,72}, the doping dependence of the charge-carrier pseudogap $\bar{\Delta}_{\text{pg}}^{(\text{h})}$ has been discussed in the detail, where the quite large $\bar{\Delta}_{\text{pg}}^{(\text{h})}$ appears in the underdoped regime, then it weakens as the doping is increased, and eventually disappears together with $\bar{\Delta}_h$ in the heavily overdoped region. In particular, at a given doping, this $\bar{\Delta}_{\text{pg}}^{(\text{h})}$ is identified as a crossover with a charge-carrier pseudogap crossover temperature T_h^* , and then in conformity with the doping dependence of $\bar{\Delta}_{\text{pg}}^{(\text{h})}$, T_h^* is quite high at the underdoped regime, and then it smoothly decreases with the increase of doping, eventually terminating together with $T_c^{(\text{pair})}$ at the heavily

overdoped region^{56,72}. More importantly, as the case of the electron pairing state, the normal-state pseudogap state originated from the charge-carrier pseudogap state is also due to the charge-spin recombination⁷³, and we will return to the discussion of the normal-state pseudogap towards subsection A 6.

6. Full charge-spin recombination

For the investigation of the low-energy electronic structure of the cuprate superconductors in the SC-state, we need to derive the full electron diagonal and off-diagonal propagators $G(\mathbf{k}, \omega)$ and $\Im^\dagger(\mathbf{k}, \omega)$ in Eq. (3) of the main text. In the previous studies⁷³, the theory of the full charge-spin recombination has been established, where a charge carrier and a localized spin are fully recombined into a constrained electron. In particular, within this framework of the full charge-spin recombination⁷³, it has been realized that the coupling form between the electrons and spin excitations is the same as the form between the charge carriers and spin excitations, which implies that the form of the self-consistent equations satisfied by the full electron diagonal and off-diagonal propagators is the same as that satisfied by the full charge-carrier diagonal and off-diagonal propagators. Following these previous discussions⁷³, we can perform a full charge-spin recombination in which the full charge-carrier diagonal and off-diagonal propagators $g(\mathbf{k}, \omega)$ and $\Gamma^\dagger(\mathbf{k}, \omega)$ in Eq. (A8) are respectively replaced by the full electron diagonal and off-diagonal propagators $G(\mathbf{k}, \omega)$ and $\Im^\dagger(\mathbf{k}, \omega)$, and then the self-consistent equations satisfied by the full electron diagonal and off-diagonal propagators of the t - J model (1) in the SC-state can be obtained straightforwardly as,

$$G(\mathbf{k}, \omega) = G^{(0)}(\mathbf{k}, \omega) + G^{(0)}(\mathbf{k}, \omega)[\Sigma_{\text{ph}}(\mathbf{k}, \omega)G(\mathbf{k}, \omega) - \Sigma_{\text{pp}}(\mathbf{k}, \omega)\Im^\dagger(\mathbf{k}, \omega)], \quad (\text{A22a})$$

$$\Im^\dagger(\mathbf{k}, \omega) = G^{(0)}(\mathbf{k}, -\omega)[\Sigma_{\text{ph}}(\mathbf{k}, -\omega)\Im^\dagger(\mathbf{k}, \omega) + \Sigma_{\text{pp}}(\mathbf{k}, \omega)G(\mathbf{k}, \omega)], \quad (\text{A22b})$$

with the electron diagonal propagator $G^{(0)}(\mathbf{k}, \omega)$ of the t - J model (1) in the tight-binding approximation,

$$G^{(0)}(\mathbf{k}, \omega) = \frac{1}{\omega - \varepsilon_{\mathbf{k}}}, \quad (\text{A23})$$

and then the full electron diagonal and off-diagonal propagators can be expressed explicitly as,

$$G(\mathbf{k}, \omega) = \frac{1}{\omega - \varepsilon_{\mathbf{k}} - \Sigma_{\text{tot}}(\mathbf{k}, \omega)}, \quad (\text{A24a})$$

$$\Im^\dagger(\mathbf{k}, \omega) = \frac{W(\mathbf{k}, \omega)}{\omega - \varepsilon_{\mathbf{k}} - \Sigma_{\text{tot}}(\mathbf{k}, \omega)}, \quad (\text{A24b})$$

as quoted in Eq. (3) of the main text, while the electron normal self-energy $\Sigma_{\text{ph}}(\mathbf{k}, \omega)$ in the particle-hole channel and the electron anomalous self-energy $\Sigma_{\text{pp}}(\mathbf{k}, \omega)$ in the

particle-particle channel are respectively obtained from the corresponding parts of the charge-carrier normal self-energy $\Sigma_{\text{ph}}^{(\text{h})}(\mathbf{k}, \omega)$ in Eq. (A11a) and the charge-carrier anomalous self-energy $\Sigma_{\text{pp}}^{(\text{h})}(\mathbf{k}, \omega)$ in Eq. (A11b) by the replacement of the full charge-carrier diagonal and off-diagonal propagators $g(\mathbf{k}, \omega)$ and $\Gamma^\dagger(\mathbf{k}, \omega)$ with the corresponding full electron diagonal and off-diagonal propagators $G(\mathbf{k}, \omega)$ and $\mathfrak{S}^\dagger(\mathbf{k}, \omega)$. However, in the previous discussions^{46–48}, the calculations of the electron normal and anomalous self-energies suffer from ignoring the vertex correction. For a better description of the anomalous properties of the cuprate superconductors, the electron normal and anomalous self-energies have been re-derived in the recent studies⁷⁶ by taking into account the vertex correction, and the calculated results show that the vertex correction functions are energy and momentum dependent. However, in this paper, as a qualitative discussion of the anomalous properties of the electronic state in the case for the low-energy close to EFS, the vertex corrections for the electron normal and anomalous self-energies can be discussed in the static limit, and then the electron normal and anomalous self-energies are respectively calculated as,

$$\begin{aligned} \Sigma_{\text{ph}}(\mathbf{k}, i\omega_n) &= \frac{1}{N^2} \sum_{\mathbf{p}, \mathbf{p}'} [V_{\text{ph}} \Lambda_{\mathbf{p}+\mathbf{p}'+\mathbf{k}}]^2 \\ &\times \frac{1}{\beta} \sum_{ip_m} G(\mathbf{p} + \mathbf{k}, ip_m + i\omega_n) \Pi(\mathbf{p}, \mathbf{p}', ip_m), \end{aligned} \quad (\text{A25a})$$

$$\begin{aligned} \Sigma_{\text{pp}}(\mathbf{k}, i\omega_n) &= \frac{1}{N^2} \sum_{\mathbf{p}, \mathbf{p}'} [V_{\text{pp}} \Lambda_{\mathbf{p}+\mathbf{p}'+\mathbf{k}}]^2 \\ &\times \frac{1}{\beta} \sum_{ip_m} \mathfrak{S}^\dagger(\mathbf{p} + \mathbf{k}, ip_m + i\omega_n) \Pi(\mathbf{p}, \mathbf{p}', ip_m), \end{aligned} \quad (\text{A25b})$$

as quoted in Eq. (5) of the main text.

The calculation process of the electron normal and anomalous self-energies is the same as that of the charge-carrier normal and anomalous self-energies in subsection A 2, i.e., the electron normal self-energy $\Sigma_{\text{ph}}(\mathbf{k}, \omega)$ is separated into its symmetric and antisymmetric parts as: $\Sigma_{\text{ph}}(\mathbf{k}, \omega) = \Sigma_{\text{phe}}(\mathbf{k}, \omega) + \omega \Sigma_{\text{pho}}(\mathbf{k}, \omega)$, and then both the symmetric part $\Sigma_{\text{phe}}(\mathbf{k}, \omega)$ and antisymmetric part $\Sigma_{\text{pho}}(\mathbf{k}, \omega)$ are an even function of energy. However, this

antisymmetric part $\Sigma_{\text{pho}}(\mathbf{k}, \omega)$ is identified as the single-particle coherent weight: $Z_{\text{F}}^{-1}(\mathbf{k}, \omega) = 1 - \text{Re}\Sigma_{\text{pho}}(\mathbf{k}, \omega)$. In an interacting system, everything happens near EFS. In the case of the discussions of the low-energy electronic structure, the electron pair gap and single-particle coherent weight can be discussed in the static-limit as,

$$\bar{\Delta}_{\mathbf{k}} = \bar{\Delta} \gamma_{\mathbf{k}}^{(\text{d})}, \quad (\text{A26a})$$

$$\frac{1}{Z_{\text{F}}} = 1 - \text{Re}\Sigma_{\text{pho}}(\mathbf{k}, 0) |_{\mathbf{k}=[\pi, 0]}, \quad (\text{A26b})$$

where the wave vector \mathbf{k} in $Z_{\text{F}}(\mathbf{k})$ has been chosen as $\mathbf{k} = [\pi, 0]$ just as it has been done in the ARPES experiments^{106,107}.

With the help of the above the electron pair gap $\bar{\Delta}_{\mathbf{k}}$ and single-particle coherent weight Z_{F} in Eq. (A26), the renormalized electron diagonal and off-diagonal propagators now can be calculated from Eq. (A22) as,

$$G^{(\text{RMF})}(\mathbf{k}, \omega) = Z_{\text{F}} \left(\frac{U_{\mathbf{k}}^2}{\omega - E_{\mathbf{k}}} + \frac{V_{\mathbf{k}}^2}{\omega + E_{\mathbf{k}}} \right), \quad (\text{A27a})$$

$$\mathfrak{S}^{(\text{RMF})\dagger}(\mathbf{k}, \omega) = -Z_{\text{F}} \frac{\bar{\Delta}_{\mathbf{z}\mathbf{k}}}{2E_{\mathbf{k}}} \left(\frac{1}{\omega - E_{\mathbf{k}}} - \frac{1}{\omega + E_{\mathbf{k}}} \right), \quad (\text{A27b})$$

where the renormalized electron energy dispersion $\bar{\varepsilon}_{\mathbf{k}} = Z_{\text{F}} \varepsilon_{\mathbf{k}}$, the renormalized electron pair gap $\bar{\Delta}_{\mathbf{z}\mathbf{k}} = Z_{\text{F}} \Delta_{\mathbf{z}\mathbf{k}}$, the SC quasiparticle energy dispersion $E_{\mathbf{k}} = \sqrt{\bar{\varepsilon}_{\mathbf{k}}^2 + |\bar{\Delta}_{\mathbf{z}\mathbf{k}}|^2}$, and the quasiparticle coherence factors

$$U_{\mathbf{k}}^2 = \frac{1}{2} \left(1 + \frac{\bar{\varepsilon}_{\mathbf{k}}}{E_{\mathbf{k}}} \right), \quad (\text{A28a})$$

$$V_{\mathbf{k}}^2 = \frac{1}{2} \left(1 - \frac{\bar{\varepsilon}_{\mathbf{k}}}{E_{\mathbf{k}}} \right), \quad (\text{A28b})$$

with the constraint $U_{\mathbf{k}}^2 + V_{\mathbf{k}}^2 = 1$ for any wave vector \mathbf{k} . The above results in Eqs. (A27) and (A28) are the standard BCS expressions for the SC-state^{1,2}, although the electron pairing mechanism is driven by the kinetic energy by the exchange of the spin excitation^{56,71–73}.

Substituting above renormalized electron diagonal and off-diagonal propagators in Eq. (A27) and spin propagator in Eq. (A5a) into Eqs. (A25), the electron normal and anomalous self-energies now can be derived as,

$$\begin{aligned} \Sigma_{\text{ph}}(\mathbf{k}, \omega) &= \frac{Z_{\text{F}}}{N^2} \sum_{\mathbf{p}\mathbf{p}'\nu} (-1)^{\nu+1} V_{\text{ph}}^2 \Omega_{\mathbf{p}\mathbf{p}'\mathbf{k}} \left[U_{\mathbf{p}+\mathbf{k}}^2 \left(\frac{F_{1\nu}(\mathbf{p}, \mathbf{p}', \mathbf{k})}{\omega + \omega_{\mathbf{p}\mathbf{p}'}^{(\nu)} - E_{\mathbf{p}+\mathbf{k}}} - \frac{F_{2\nu}(\mathbf{p}, \mathbf{p}', \mathbf{k})}{\omega - \omega_{\mathbf{p}\mathbf{p}'}^{(\nu)} - E_{\mathbf{p}+\mathbf{k}}} \right) \right. \\ &\quad \left. + V_{\mathbf{p}+\mathbf{k}}^2 \left(\frac{F_{1\nu}(\mathbf{p}, \mathbf{p}', \mathbf{k})}{\omega - \omega_{\mathbf{p}\mathbf{p}'}^{(\nu)} + E_{\mathbf{p}+\mathbf{k}}} - \frac{F_{2\nu}(\mathbf{p}, \mathbf{p}', \mathbf{k})}{\omega + \omega_{\mathbf{p}\mathbf{p}'}^{(\nu)} + E_{\mathbf{p}+\mathbf{k}}} \right) \right], \end{aligned} \quad (\text{A29a})$$

$$\begin{aligned} \Sigma_{\text{pp}}(\mathbf{k}, \omega) = & \frac{Z_{\text{F}}}{N^2} \sum_{\mathbf{pp}'\nu} (-1)^\nu V_{\text{pp}}^2 \Omega_{\mathbf{pp}'\mathbf{k}} \frac{\bar{\Delta}_{\text{Z}}(\mathbf{p} + \mathbf{k})}{2E_{\mathbf{p}+\mathbf{k}}} \left[\left(\frac{F_{1\nu}(\mathbf{p}, \mathbf{p}', \mathbf{k})}{\omega + \omega_{\mathbf{pp}'}^{(\nu)} - E_{\mathbf{p}+\mathbf{k}}} - \frac{F_{2\nu}(\mathbf{p}, \mathbf{p}', \mathbf{k})}{\omega - \omega_{\mathbf{pp}'}^{(\nu)} - E_{\mathbf{p}+\mathbf{k}}} \right) \right. \\ & \left. - \left(\frac{F_{1\nu}(\mathbf{p}, \mathbf{p}', \mathbf{k})}{\omega - \omega_{\mathbf{pp}'}^{(\nu)} + E_{\mathbf{p}+\mathbf{k}}} - \frac{F_{2\nu}(\mathbf{p}, \mathbf{p}', \mathbf{k})}{\omega + \omega_{\mathbf{pp}'}^{(\nu)} + E_{\mathbf{p}+\mathbf{k}}} \right) \right], \end{aligned} \quad (\text{A29b})$$

respectively, with $\nu = 1, 2$, and the functions,

$$F_{1\nu}(\mathbf{p}, \mathbf{p}', \mathbf{k}) = n_{\text{F}}(E_{\mathbf{p}+\mathbf{k}})\{1 + n_{\text{B}}(\omega_{\mathbf{p}'+\mathbf{p}}) + n_{\text{B}}[(-1)^{\nu+1}\omega_{\mathbf{p}'}]\} + n_{\text{B}}(\omega_{\mathbf{p}'+\mathbf{p}})n_{\text{B}}[(-1)^{\nu+1}\omega_{\mathbf{p}'}], \quad (\text{A30a})$$

$$F_{2\nu}(\mathbf{p}, \mathbf{p}', \mathbf{k}) = [1 - n_{\text{F}}(E_{\mathbf{p}+\mathbf{k}})]\{1 + n_{\text{B}}(\omega_{\mathbf{p}'+\mathbf{p}}) + n_{\text{B}}[(-1)^{\nu+1}\omega_{\mathbf{p}'}]\} + n_{\text{B}}(\omega_{\mathbf{p}'+\mathbf{p}})n_{\text{B}}[(-1)^{\nu+1}\omega_{\mathbf{p}'}]. \quad (\text{A30b})$$

As the case of the charge-carrier normal self-energy in Eq. (A21), the above electron normal self-energy in Eq. (A29a) can be also reexpressed as,

$$\Sigma_{\text{ph}}(\mathbf{k}, \omega) \approx \frac{[2\bar{\Delta}_{\text{PG}}(\mathbf{k})]^2}{\omega - \varepsilon_{\mathbf{k}}}, \quad (\text{A31})$$

as quoted in Eq. (7) of the main text.

7. Self-consistent equations for determination of electron order parameters

In the framework of the full charge-spin recombination⁷³, the electron pairing gap and the normal-state pseudogap respectively originate from the charge-carrier pairing gap and charge-carrier pseudogap. In this case, the electron pairing gap parameter and normal-state pseudogap parameter can be respectively set as $\bar{\Delta} = \bar{\Delta}_{\text{h}}$ and $\bar{\Delta}_{\text{PG}} = \bar{\Delta}_{\text{pg}}^{(\text{h})}$, and then the single-particle coherent weight, the vertex correction parameters V_{ph} and V_{pp} , and the electron chemical potential satisfy following four self-consistent equations,

$$\frac{1}{Z_{\text{F}}} = 1 + \frac{Z_{\text{F}}}{N^2} \sum_{\mathbf{pp}'\nu} (-1)^{\nu+1} V_{\text{ph}}^2 \Omega_{\mathbf{pp}'\mathbf{k}_{\text{A}}} \left(\frac{F_{1\nu}(\mathbf{p}, \mathbf{p}', \mathbf{k}_{\text{A}})}{(\omega_{\mathbf{pp}'}^{(\nu)} - E_{\mathbf{p}+\mathbf{k}_{\text{A}}})^2} + \frac{F_{2\nu}(\mathbf{p}, \mathbf{p}', \mathbf{k}_{\text{A}})}{(\omega_{\mathbf{pp}'}^{(\nu)} + E_{\mathbf{p}+\mathbf{k}_{\text{A}}})^2} \right), \quad (\text{A32a})$$

$$1 = \frac{4Z_{\text{F}}^2}{N^3} \sum_{\mathbf{pp}'\mathbf{k}\nu} (-1)^\nu V_{\text{pp}}^2 \Omega_{\mathbf{pp}'\mathbf{k}} \frac{\gamma_{\mathbf{k}}^{(\text{d})} \gamma_{\mathbf{p}+\mathbf{k}}^{(\text{d})}}{E_{\mathbf{p}+\mathbf{k}}} \left(\frac{F_{1\nu}(\mathbf{p}, \mathbf{p}', \mathbf{k})}{\omega_{\mathbf{pp}'}^{(\nu)} - E_{\mathbf{p}+\mathbf{k}}} - \frac{F_{2\nu}(\mathbf{p}, \mathbf{p}', \mathbf{k})}{\omega_{\mathbf{pp}'}^{(\nu)} + E_{\mathbf{p}+\mathbf{k}}} \right), \quad (\text{A32b})$$

$$(\bar{\Delta}_{\text{pg}}^{(\text{h})})^2 = -\frac{Z_{\text{F}}}{4N^3} \sum_{\mathbf{kpp}'\nu} (-1)^{\nu+1} V_{\text{ph}}^2 \varepsilon_{\mathbf{k}} \Omega_{\mathbf{pp}'\mathbf{k}} \frac{\bar{\varepsilon}_{\mathbf{p}+\mathbf{k}}}{E_{\mathbf{p}+\mathbf{k}}} \left(\frac{F_{1\nu}(\mathbf{p}, \mathbf{p}', \mathbf{k})}{\omega_{\mathbf{pp}'}^{(\nu)} - E_{\mathbf{p}+\mathbf{k}}} + \frac{F_{2\nu}(\mathbf{p}, \mathbf{p}', \mathbf{k})}{\omega_{\mathbf{pp}'}^{(\nu)} + E_{\mathbf{p}+\mathbf{k}}} \right), \quad (\text{A32c})$$

$$1 - \delta = \frac{Z_{\text{F}}}{2N} \sum_{\mathbf{k}} \left(1 - \frac{\bar{\varepsilon}_{\mathbf{k}}}{E_{\mathbf{k}}} \tanh \left[\frac{1}{2} \beta E_{\mathbf{k}} \right] \right), \quad (\text{A32d})$$

respectively, where $\mathbf{k}_{\text{A}} = [\pi, 0]$. Within the same calculation condition as in the evaluation of the self-consistent equations (A19) and (A20), the above self-consistent equations (A32) have been also solved simultaneously, and then the single-particle coherent weight, the vertex correction parameters, and electron chemical potential are determined *without using any adjustable parameters*. In particular, the evolution of the electron pair gap parameter $\bar{\Delta}$ and the normal-state pseudogap parameter $\bar{\Delta}_{\text{PG}}$ with doping has been derived, and the results of $\bar{\Delta}$ and $\bar{\Delta}_{\text{PG}}$ as a function of doping are plotted in Fig. 1a.

8. Electron pair transition temperature

Concomitantly, the evolution of the electron pair transition temperature T_{c} with doping can be also calculated self-consistently from the above self-consistent equations (A32) at the condition of $\bar{\Delta} = 0$, and the result⁷³ of T_{c} as a function of doping is plotted in Fig. 1b (black-line), where in a given doping, the magnitude of T_{c} is exactly identical to the corresponding magnitude^{56,72} of the charge-carrier pair transition temperature $T_{\text{c}}^{(\text{pair})}$. This follows a basic fact that in the framework of the kinetic-energy-driven superconductivity^{56,71-73}, the effective attractive interaction between charge carriers originates in their coupling to the spin excitation. On the other hand, the electron pairing interaction in the framework of the full charge-spin recombination⁷³ is mediated by the exchange of the same spin

excitation, which thus leads to that the magnitude of T_c is the same as the magnitude of the corresponding $T_c^{(\text{pair})}$, and then the dome-like shape of the doping dependence of T_c with its maximum occurring at around the optimal doping is a natural consequence of the dome-like shape of the doping dependence of $T_c^{(\text{pair})}$ with its maximum occurring at around the same optimal doping.

9. Normal-state pseudogap crossover temperature

As in the case of the temperature dependence of the electron pair gap $\bar{\Delta}$, the normal-state pseudogap $\bar{\Delta}_{\text{PG}}$ is also strongly temperature dependent. In particular, in a given doping, the normal-state pseudogap vanishes when temperature reaches the normal-state pseudogap crossover temperature T^* . In this case, we have also made a series of calculations for T^* at different doping concentrations, and the results of T^* as a function of doping is plotted in Fig. 1b (red-line).

* Corresponding author. E-mail: spfeng@bnu.edu.cn

¹ J. Bardeen, L. N. Cooper, and J. R. Schrieffer, *Phys. Rev.* **108**, 1175 (1957).

² J. R. Schrieffer, *Theory of Superconductivity*, Benjamin, New York, 1964.

³ J. G. Bednorz and K. A. Müller, *Z. Phys. B* **64**, 189 (1986).

⁴ M. K. Wu, J. R. Ashburn, C. J. Torng, P. H. Hor, R. L. Meng, L. Gao, Z. J. Huang, Y. Q. Wang, and C. W. Chu, *Phys. Rev. Lett.* **58**, 908 (1987).

⁵ See, e.g., the review, C. C. Tsuei and J. R. Kirtley, *Rev. Mod. Phys.* **72**, 969 (2000).

⁶ See, e.g., the review, A. V. Puchkov, D. N. Basov, and T. Timusk, *J. Phys.: Condens. Matter* **8**, 10049 (1996).

⁷ See, e.g., the review, T. Timusk and B. Statt, *Rep. Prog. Phys.* **62**, 61 (1999).

⁸ See, e.g., the review, S. Hufner, M. A. Hossain, A. Damascelli, and G. A. Sawatzky, *Rep. Prog. Phys.* **71**, 062501 (2008).

⁹ See, e.g., the review, N. E. Hussey, *J. Phys.: Condens. Matter* **20**, 123201 (2008); N. E. Hussey, *J. Phys. Chem. Solids* **72**, 529 (2011).

¹⁰ See, e.g., the review, A. Damascelli, Z. Hussain, and Z.-X. Shen, *Rev. Mod. Phys.* **75**, 473 (2003).

¹¹ See, e.g., the review, J. C. Campuzano, M. R. Norman, M. Randeria, in *Physics of Superconductors*, vol. II, edited by K. H. Bennemann and J. B. Ketterson (Springer, Berlin Heidelberg New York, 2004), p. 167.

¹² See, e.g., the review, J. Fink, S. Borisenko, A. Kordyuk, A. Koitzsch, J. Geck, V. Zabalotnyy, M. Knupfer, B. Büchner, and H. Berger, in *Lecture Notes in Physics*, vol. 715, edited by S. Hufner (Springer-Verlag Berlin Heidelberg, 2007), p. 295.

¹³ J. Zaanen, *Nature* **430**, 512 (2004).

¹⁴ N. Barišić, M. K. Chan, Y. Li, G. Yu, X. Zhao, M. Dressel, A. Smontara, and M. Greven, *Proc. Natl. Acad. Sci. USA* **110**, 12235 (2013).

¹⁵ See, e.g., the review, B. Keimer, S. A. Kivelson, M. R. Norman, S. Uchida, and J. Zaanen, *Nature* **518**, 179 (2015).

¹⁶ See, e.g., the review, I. M. Vishik, *Rep. Prog. Phys.* **81**, 062501 (2018).

¹⁷ M. R. Norman, H. Ding, M. Randeria, J. C. Campuzano,

T. Yokoya, T. Takeuchi, T. Takahashi, T. Mochiku, K. Kadowaki, P. Guptasarma, and D. G. Hinks, *Nature* **392**, 157 (1998).

¹⁸ T. Yoshida, X. J. Zhou, K. Tanaka, W. L. Yang, Z. Hussain, Z.-X. Shen, A. Fujimori, S. Sahrakorpi, M. Lindroos, R. S. Markiewicz, A. Bansil, S. Komiya, Y. Ando, H. Eisaki, T. Kakeshita, and S. Uchida, *Phys. Rev. B* **74**, 224510 (2006).

¹⁹ K. Tanaka, W. S. Lee, D. H. Lu, A. Fujimori, T. Fujii, Risdiana, I. Terasaki, D. J. Scalapino, T. P. Devereaux, Z. Hussain, and Z.-X. Shen, *Science* **314**, 1910 (2006).

²⁰ A. Kanigel, U. Chatterjee, M. Randeria, M. R. Norman, S. Souma, M. Shi, Z. Z. Li, H. Raffy, and J. C. Campuzano, *Phys. Rev. Lett.* **99**, 157001 (2007).

²¹ M. Shi, J. Chang, S. Pailh s, M. R. Norman, J. C. Campuzano, M. M nsson, T. Claesson, O. Tjernberg, A. Bendounan, L. Patthey, N. Momono, M. Oda, M. Ido, C. Mudry, and J. Mesot, *Phys. Rev. Lett.* **101**, 047002 (2008).

²² Y. Sassa, M. Radovi c, M. M nsson, E. Razzoli, X. Y. Cui, S. Pailh s, S. Guerrero, M. Shi, P. R. Willmott, F. Miletto Granozio, J. Mesot, M. R. Norman, and L. Patthey, *Phys. Rev. B* **83**, 140511(R) (2011).

²³ M. Horio, T. Adachi, Y. Mori, A. Takahashi, T. Yoshida, H. Suzuki, L. C. C. Amolode II, K. Okazaki, K. Ono, H. Kumigashira, H. Anzai, M. Arita, H. Namatame, M. Taniguchi, D. Ootsuki, K. Sawada, M. Takahashi, T. Mizokawa, Y. Koike, and A. Fujimori, *Nat. Commun.* **7**, 10567 (2016).

²⁴ B. Lorent, Y. Gallais, M. Cazayous, R. D. Zhong, J. Schneeloch, G. D. Gu, A. Fedorov, T. K. Kim, S. V. Borisenko, and A. Sacuto, *Phys. Rev. B* **97**, 174521 (2018).

²⁵ R. Comin, A. Frano, M. M. Yee, Y. Yoshida, H. Eisaki, E. Schierle, E. Weschke, R. Sutarto, F. He, A. Soumyanarayanan, Y. He, M. L. Tacon, I. S. Elfimov, Jennifer E. Hoffman, G. A. Sawatzky, B. Keimer, and A. Damascelli, *Science* **343**, 390 (2014).

²⁶ G. Ghiringhelli, M. L. Tacon, M. Minola, S. Blanco-Canosa, G. Mazzoli, N. B. Brookes, G. M. D. Luca, A. Frano, D. G. Hawthorn, F. He, T. Loew, M. M. Sala, D. C. Peets, M. Salluzzo, E. Schierle, R. Sutarto, G. A. Sawatzky, E. Weschke, B. Keimer, and L. Braicovich, *Sci-*

- ence **337** (2012) 821.
- ²⁷ E. H. da Silva Neto, P. Aynajian, A. Frano, R. Comin, E. Schierle, E. Weschke, A. Gyenis, J. Wen, J. Schneeloch, Z. Xu, S. Ono, G. Gu, M. L. Tacon, and A. Yazdani, *Science* **343** (2014) 393.
- ²⁸ M. Hashimoto, E. A. Nowadnick, R.-H. He, I. M. Vishik, B. Moritz, Y. He, K. Tanaka, R. G. Moore, D. Lu, Y. Yoshida, M. Ishikado, T. Sasagawa, K. Fujita, S. Ishida, S. Uchida, H. Eisaki, Z. Hussain, T. P. Devereaux, and Z.-X. Shen, *Nat. Mater.* **14** (2015) 37.
- ²⁹ See, e.g., the review, R. Comin, A. Damascelli, *Annu. Rev. Condens. Matter Phys.* **7**, 369 (2016).
- ³⁰ G. Campi, A. Bianconi, N. Poccia, G. Bianconi, L. Barba, G. Arrighetti, D. Innocenti, J. Karpinski, N. D. Zhigadlo, S. M. Kazakov, M. Burghammer, M. v. Zimmermann, M. Sprung and A. Ricci, *Nature* **525**, 359 (2015).
- ³¹ D. S. Dessau, B. O. Wells, Z.-X. Shen, W. E. Spicer, A. J. Arko, R. S. List, D. B. Mitzi, and A. Kapitulnik, *Phys. Rev. Lett.* **66**, 2160 (1991).
- ³² J. C. Campuzano, H. Ding, M. R. Norman, H. M. Fretwell, M. Randeria, A. Kaminski, J. Mesot, T. Takeuchi, T. Sato, T. Yokoya, T. Takahashi, T. Mochiku, K. Kadowaki, P. Guptasarma, D. G. Hinks, Z. Konstantinovic, Z. Z. Li, and H. Raffy, *Phys. Rev. Lett.* **83**, 3709 (1999).
- ³³ D. H. Lu, D. L. Feng, N. P. Armitage, K. M. Shen, A. Damascelli, C. Kim, F. Ronning, Z.-X. Shen, D. A. Bonn, R. Liang, W. N. Hardy, A. I. Rykov, and S. Tajima, *Phys. Rev. Lett.* **86**, 4370 (2001).
- ³⁴ T. Sato, H. Matsui, S. Nishina, T. Takahashi, T. Fujii, T. Watanabe, and A. Matsuda, *Phys. Rev. Lett.* **89**, 067005 (2002).
- ³⁵ S. V. Borisenko, A. A. Kordyuk, T. K. Kim, A. Koitzsch, M. Knupfer, M. S. Golden, J. Fink, M. Eschrig, H. Berger, and R. Follath, *Phys. Rev. Lett.* **90**, 207001 (2003).
- ³⁶ J. Wei, Y. Zhang, H. W. Ou, B. P. Xie, D. W. Shen, J. F. Zhao, L. X. Yang, M. Arita, K. Shimada, H. Namatame, M. Taniguchi, Y. Yoshida, H. Eisaki, and D. L. Feng, *Phys. Rev. Lett.* **101**, 097005 (2008).
- ³⁷ S. Sakai, S. Blanc, M. Civelli, Y. Gallais, M. Cazayous, M.-A. Méasson, J. S. Wen, Z. J. Xu, G. D. Gu, G. Sangiovanni, Y. Motome, K. Held, A. Sacuto, A. Georges, and M. Imada, *Phys. Rev. Lett.* **111**, 107001 (2013).
- ³⁸ M. Hashimoto, E. A. Nowadnick, R.-H. He, I. M. Vishik, B. Moritz, Y. He, K. Tanaka, R. G. Moore, D. Lu, Y. Yoshida, M. Ishikado, T. Sasagawa, K. Fujita, S. Ishida, S. Uchida, H. Eisaki, Z. Hussain, T. P. Devereaux, and Z.-X. Shen, *Nat. Mater.* **14**, 37 (2015).
- ³⁹ B. Loret, S. Sakai, S. Benhabib, Y. Gallais, M. Cazayous, M. A. Méasson, R. D. Zhong, J. Schneeloch, G. D. Gu, A. Forget, D. Colson, I. Paul, M. Civelli, and A. Sacuto, *Phys. Rev. B* **96**, 094525 (2017).
- ⁴⁰ D. Mou, A. Kaminski, and G. Gu, *Phys. Rev. B* **95**, 174501 (2017).
- ⁴¹ U. Chatterjee, M. Shi, A. Kaminski, A. Kanigel, H. M. Fretwell, K. Terashima, T. Takahashi, S. Rosenkranz, Z. Z. Li, H. Raffy, A. Santander-Syro, K. Kadowaki, M. R. Norman, M. Randeria, and J. C. Campuzano, *Phys. Rev. Lett.* **96**, 107006 (2006).
- ⁴² Y. He, Y. Yin, M. Zech, A. Soumyanarayanan, M. M. Yee, T. Williams, M. C. Boyer, K. Chatterjee, W. D. Wise, I. Zeljkovic, T. Kondo, T. Takeuchi, H. Ikuta, P. Mistark, R. S. Markiewicz, A. Bansil, S. Sachdev, E. W. Hudson, and J. E. Hoffman, *Science* **344**, 608 (2014).
- ⁴³ F. Restrepo, J. Zhao, J. C. Campuzano, and U. Chatterjee, *Phys. Rev. B* **107**, 174519 (2023).
- ⁴⁴ See, e.g., the review, J. P. Carbotte, T. Timusk, and J. Hwang, *Rep. Prog. Phys.* **74**, 066501 (2011).
- ⁴⁵ J. M. Bok, J. J. Bae, H.-Y. Choi, C. M. Varma, W. Zhang, J. He, Y. Zhang, L. Yu, and X. J. Zhou, *Sci. Adv.* **2**, e1501329 (2016).
- ⁴⁶ S. Feng, D. Gao, and H. Zhao, *Phil. Mag.* **96**, 1245 (2016).
- ⁴⁷ D. Gao, Y. Mou, and S. Feng, *J. Low Temp. Phys.* **192**, 19 (2018).
- ⁴⁸ D. Gao, Y. Mou, Y. Liu, S. Tan, and S. Feng, *Phil. Mag.* **99**, 752 (2019).
- ⁴⁹ P. W. Anderson, *Science* **235**, 1196 (1987).
- ⁵⁰ See, e.g., the review, L. Yu, in *Recent Progress in Many-Body Theories*, edited by T. L. Ainsworth, C. E. Campbell, B. E. Clements, and E. Krotscheck (Plenum, New York, 1992), Vol. **3**, p. 157, and references therein.
- ⁵¹ S. Feng, J. B. Wu, Z. B. Su, and L. Yu, *Phys. Rev. B* **47**, 15192 (1993), and references therein.
- ⁵² L. Zhang, J. K. Jain, and V. J. Emery, *Phys. Rev. B* **47**, 3368 (1993), and references therein.
- ⁵³ See, e.g., the review, P. A. Lee, N. Nagaosa, and X.-G. Wen, *Rev. Mod. Phys.* **78**, 17 (2006), and references therein.
- ⁵⁴ J. Spalek, M. Fidrysiak, M. Zegrodnik, and A. Biborski, *Phys. Rep.* **959**, 1 (2022), and references therein.
- ⁵⁵ S. Feng, J. Qin, and T. Ma, *J. Phys.: Condens. Matter* **16**, 343 (2004); S. Feng, Z. B. Su, and L. Yu, *Phys. Rev. B* **49**, 2368 (1994).
- ⁵⁶ See, e.g., the review, S. Feng, Y. Lan, H. Zhao, L. Kuang, L. Qin, and X. Ma, *Int. J. Mod. Phys. B* **29**, 1530009 (2015).
- ⁵⁷ P. W. Anderson, *Science* **317**, 1705 (2007).
- ⁵⁸ L. N. Cooper, *Phys. Rev.* **104**, 1189 (1956).
- ⁵⁹ P. Monthoux, D. Pines, and G. G. Lonzarich, *Nature* **450**, 1177 (2007).
- ⁶⁰ J. L. Miller, *Phys. Today* **64**, 13 (2011).
- ⁶¹ See, e.g., the review, M. Fujita, H. Hiraka, M. Matsuda, M. Matsuura, J. M. Tranquada, S. Wakimoto, G. Xu, and K. Yamada, *J. Phys. Soc. Jpn.* **81**, 011007 (2012).
- ⁶² R. J. Birgeneau, Y. Endoh, K. Kakurai, Y. Hidaka, T. Murakami, M. A. Kastner, T. R. Thurston, G. Shirane, and K. Yamada, *Phys. Rev. B* **39**, 2868 (1989).
- ⁶³ H. F. Fong, B. Keimer, P. W. Anderson, D. Reznik, F. Doğan, and I. A. Aksay, *Phys. Rev. Lett.* **75**, 316 (1995).
- ⁶⁴ K. Yamada, C. H. Lee, K. Kurahashi, J. Wada, S. Wakimoto, S. Ueki, H. Kimura, Y. Endoh, S. Hosoya, G. Shirane, R. J. Birgeneau, M. Greven, M. A. Kastner, and Y. J. Kim, *Phys. Rev. B* **57**, 6165 (1998).
- ⁶⁵ M. Arai, T. Nishijima, Y. Endoh, T. Egami, S. Tajima, K. Tomimoto, Y. Shiohara, M. Takahashi, A. Garret, and S. M. Bennington, *Phys. Rev. Lett.* **83**, 608 (1999).
- ⁶⁶ P. Bourges, Y. Sidis, H. F. Fong, L. P. Regnault, J. Bossy, A. Ivanov, and B. Keimer, *Science* **288**, 1234 (2000).
- ⁶⁷ H. He, Y. Sidis, P. Bourges, G. D. Gu, A. Ivanov, N. Koshizuka, B. Liang, C. T. Lin, L. P. Regnault, E. Schoenher, and B. Keimer, *Phys. Rev. Lett.* **86**, 1610 (2001); S. M. Hayden, H. A. Mook, P. Dai, T. G. Perring, and F. Doğan, *Nature* **429**, 531 (2004).
- ⁶⁸ J. M. Tranquada, H. Woo, T. G. Perring, H. Goka, G. D. Gu, G. Xu, M. Fujita, and K. Yamada, *Nature* **429**, 534 (2004).
- ⁶⁹ Ph. Bourges, B. Keimer, S. Pailhès, L. P. Regnault, Y. Sidis, and C. Ulrich, *Physica C* **424**, 45 (2005).
- ⁷⁰ See, e.g., the review, M. P. M. Dean, *J. Magn. Magn.*

- Mater. **376**, 3 (2015).
- ⁷¹ S. Feng, Phys. Rev. B **68**, 184501 (2003); S. Feng, T. Ma, and H. Guo, Physica C **436**, 14 (2006).
- ⁷² S. Feng, H. Zhao, and Z. Huang, Phys. Rev. B. **85**, 054509 (2012); Phys. Rev. B. **85**, 099902(E) (2012).
- ⁷³ S. Feng, L. Kuang, and H. Zhao, Physica C **517**, 5 (2015).
- ⁷⁴ J. R. Schrieffer, J. Low Temp. Phys. **99**, 397 (1995).
- ⁷⁵ K.-J. Xu, Q. Guo, M. Hashimoto, Z.-X. Li, S.-D. Chen, J. He, Y. He, C. Li, M. H. Berntsen, C. R. Rotundu, Y. S. Lee, T. P. Devereaux, A. Rydh, D.-H. Lu, D.-H. Lee, O. Tjernberg, Z.-X. Shen, Nat. Phys. **19**, 1834 (2023).
- ⁷⁶ M. Zeng, X. Li, H. Guo, and S. Feng, unpublished.
- ⁷⁷ J. Brinckmann and P. A. Lee, Phys. Rev. B **65**, 014502 (2001).
- ⁷⁸ V. J. Emery and S. A. Kivelson, Nature **374**, 434 (1995).
- ⁷⁹ T. Kondo, R. Khasanov, T. Takeuchi, J. Schmalian, and A. Kaminski, Nature **457**, 296 (2009).
- ⁸⁰ Z. Tešanović, Nat. Phys. **4**, 408 (2008).
- ⁸¹ L. Benfatto, S. Caprara, and C. D. Castro, Eur. Phys. J. B **17**, 95 (2000).
- ⁸² A. Cho, Science **314**, 1072 (2006).
- ⁸³ A. J. Millis, Science **314**, 1888 (2006).
- ⁸⁴ See, e.g., the review, T. M. Rice, K. Y. Yang, and F. C. Zhang, Rep. Prog. Phys. **75**, 016502 (2012).
- ⁸⁵ C. E. Matt, C. G. Fatuzzo, Y. Sassa, M. Mansson, S. Fatale, V. Bitetta, X. Shi, S. Pailhes, M. H. Berntsen, T. Kurosawa, M. Oda, N. Momono, O. J. Lipscombe, S. M. Hayden, J.-Q. Yan, J.-S. Zhou, J. B. Goodenough, S. Pyon, T. Takayama, H. Takagi, L. Patthey, A. Bendounan, E. Razzoli, M. Shi, N.C. Plumb, M. Radovic, M. Grioni, J. Mesot, O. Tjernberg, and J. Chang, Phys. Rev. B **92**, 134524 (2015).
- ⁸⁶ Y. Liu, Y. Lan, and S. Feng, Phys. Rev. B **103**, 024525 (2021); S. Tan, Y. Liu, Y. Mou, and S. Feng, Phys. Rev. B **103**, 014503 (2021).
- ⁸⁷ Z. Cao, Y. Liu, H. Guo, and S. Feng, Phil. Mag. **102**, 918 (2022); M. Zeng, X. Li, Y. Wang, and S. Feng, Phys. Rev. B **106**, 054512 (2022).
- ⁸⁸ J. E. Hoffman, K. McElroy, D.-H. Lee, K. M. Lang, H. Eisaki, S. Uchida, and J. C. Davis, Science **297**, 1148 (2002).
- ⁸⁹ K. McElroy, R. W. Simmonds, J. E. Hoffman, D.-H. Lee, J. Orenstein, H. Eisaki, S. Uchida, and J. C. Davis, Nature **422**, 592 (2003).
- ⁹⁰ J.-X. Yin, S. H. Pan, M. Z. Hasan, Nat. Rev. Phys. **3**, 249 (2021).
- ⁹¹ S. H. Pan, E. W. Hudson, K. M. Lang, H. Eisaki, S. Uchida, and J. C. Davis, Nature **403**, 746 (2000).
- ⁹² Y. Kohsaka, C. Taylor, P. Wahl, A. Schmidt, J. Lee, K. Fujita, J. W. Alldredge, K. McElroy, J. Lee, H. Eisaki, S. Uchida, D.-H. Lee, and J. C. Davis, Nature **454**, 1072 (2008).
- ⁹³ T. Hanaguri, Y. Kohsaka, M. Ono, M. Maltseva, P. Coleman, I. Yamada, M. Azuma, M. Takano, K. Ohishi, and H. Takagi, Science **323**, 923 (2009).
- ⁹⁴ J. Lee, K. Fujita, A. R. Schmidt, C. K. Kim, H. Eisaki, S. Uchida, and J. C. Davis, Science **325**, 1099 (2009).
- ⁹⁵ I. M. Vishik, E. A. Nowadnick, W. S. Lee, Z. X. Shen, B. Moritz, T. P. Devereaux, K. Tanaka, T. Sasagawa, and T. Fujii, Nat. Phys. **5**, 718 (2009).
- ⁹⁶ A. R. Schmidt, K. Fujita, E.-A. Kim, M. J. Lawler, H. Eisaki, S. Uchida, D.-H. Lee, and J. C. Davis, New J. Phys. **13**, 065014 (2011).
- ⁹⁷ K. M. Shen, F. Ronning, D. H. Lu, F. Baumberger, N. J. C. Ingle, W. S. Lee, W. Meevasana, Y. Kohsaka, M. Azuma, M. Takano, H. Takagi, and Z.-X. Shen, Science **307**, 901 (2005).
- ⁹⁸ M. Vershinin, S. Misra, S. Ono, Y. Abe, Y. Ando, and A. Yazdani, Science **303**, 1995 (2004).
- ⁹⁹ T. Hanaguri, C. Lupien, Y. Kohsaka, D.-H. Lee, M. Azuma, M. Takano, H. Takagi, and J. C. Davis, Nature **430**, 1001 (2004).
- ¹⁰⁰ K. McElroy, D.-H. Lee, J. E. Hoffman, K. M. Lang, J. Lee, E. W. Hudson, H. Eisaki, S. Uchida, and J. C. Davis, Phys. Rev. Lett. **94**, 197005 (2005).
- ¹⁰¹ W. D. Wise, M. C. Boyer, K. Chatterjee, T. Kondo, T. Takeuchi, H. Ikuta, Y. Wang, E. W. Hudson, Nat. Phys. **4**, 696 (2008).
- ¹⁰² K. McElroy, G.-H. Gweon, S. Y. Zhou, J. Graf, S. Uchida, H. Eisaki, H. Takagi, T. Sasagawa, D.-H. Lee, and A. Lanzara, Phys. Rev. Lett. **96**, 067005 (2006).
- ¹⁰³ X. Li, M. Zeng, H. Guo, and S. Feng, unpublished.
- ¹⁰⁴ J. Kondo and K. Yamaji, Prog. Theor. Phys. **47**, 807 (1972).
- ¹⁰⁵ See, e.g., S. V. Tyablikov, *Method in the Quantum Theory of Magnetism* (Plenum, New York, 1967).
- ¹⁰⁶ D. L. Feng, D. H. Lu, K. M. Shen, C. Kim, H. Eisaki, A. Damascelli, R. Yoshizaki, J.-i. Shimoyama, K. Kishio, G. D. Gu, S. Oh, A. Andrus, J. O'Donnell, J. N. Eckstein, and Z.-X. Shen, Science **289**, 277 (2000).
- ¹⁰⁷ H. Ding, J. R. Engelbrecht, Z. Wang, J. C. Campuzano, S.-C. Wang, H.-B. Yang, R. Rogan, T. Takahashi, K. Kadowaki, and D. G. Hinks, Phys. Rev. Lett. **87**, 227001 (2001).